

## Mesoscale Structural Evolution of Three Tropical Weather Systems Observed during PREDICT

CHRISTOPHER A. DAVIS AND DAVID A. AHIEVYCH

*National Center for Atmospheric Research,\* Boulder, Colorado*

(Manuscript received 23 August 2011, in final form 10 November 2011)

### ABSTRACT

Three well-observed Atlantic tropical weather systems that occurred during the 2010 hurricane season are analyzed. One case was former Tropical Storm Gaston that failed to redevelop into a tropical cyclone; the other two cases were developing storms Karl and Matthew. Geostationary satellite, multisensor-derived precipitation, and dropsondes from the National Science Foundation (NSF)-NCAR Gulfstream V (GV), NASA DC-8, and the NOAA Gulfstream IV (G-IV) and WP-3D Orion (P-3) aircraft are analyzed in a system-following frame to quantify the mesoscale dynamics of these systems.

Gaston featured extensive dry air surrounding an initially moist core. Vertical shear forced a misalignment of midtropospheric and lower-tropospheric circulation centers. This misalignment allowed dry air to intrude above the lower-tropospheric center and severely limited the area influenced by deep moist convection, thus providing little chance of maintaining or rebuilding the vortex in sheared flow. By contrast, Karl and Matthew developed in a moister environment overall, with moisture increasing with time in the middle and upper troposphere. Deep moist convection was quasi-diurnal prior to genesis. For Karl, deep convection was initially organized away from the lower-tropospheric circulation center, creating a misalignment of the vortex. The vortex gradually realigned over several days and genesis followed this realignment within roughly one day. Matthew experienced weaker shear, was vertically aligned through most of its early evolution, and developed more rapidly than Karl. The evolutions of the three cases are interpreted in the context of recent theories of tropical cyclone formation.

### 1. Introduction

The continued interest in understanding the mechanisms governing tropical cyclone (TC) formation arises in large part because of the elusiveness of observations leading up to the time of formation, combined with the need to properly represent these processes in numerical forecasts and in climate models. There are numerous summaries in the literature of the scientific issues concerning the process of TC formation, which herein is synonymous with the term “genesis” and refers to the formation of a tropical depression. Rather comprehensive summaries appear in Gray (1998), Halverson et al. (2007), Dunkerton et al. (2009, hereafter D09), and Tory

and Frank (2010). Some important points from relatively recent articles are discussed below.

Numerous theories have been advanced, particularly in the most recent 15 years, to explain the formation of a tropical cyclone. In general, the theories are somewhat intertwined in pointing to several important processes that determine which disturbances are more likely to develop.<sup>1</sup> For instance, Bister and Emanuel (1997) invoke the stratiform rain region of tropical mesoscale convective systems to moisten the lower and middle troposphere, slightly cool the column, and gradually lower the cyclonic circulation. Simpson et al. (1997) and Ritchie and Holland (1997) propose that strengthening the midtropospheric

\* The National Center for Atmospheric Research is sponsored by the National Science Foundation.

Corresponding author address: Christopher A. Davis, NCAR, P.O. Box 3000, Boulder, CO 80307.  
E-mail: cdavis@ucar.edu

<sup>1</sup> Herein, words such as *formation* and *development* refer to the intensification of a tropical weather system into a tropical depression as designated by the National Hurricane Center. While there is no unambiguous intensity or structural definition of a tropical depression, it usually represents a disturbance with organized deep moist convection and maximum sustained surface winds of 25–30 kt (12.9–15.4 m s<sup>-1</sup>).

cyclonic circulation through vortex merger could enhance the cyclonic circulation in the boundary layer through vertical penetration even if the potential vorticity anomaly continues to reside in the middle troposphere.<sup>2</sup> Both of these conceptual pathways result in a pregenesis vortex profile in which the cyclonic circulation increases with height, and in thermal wind balance is consistent with a negative temperature anomaly (relative to the quiescent environment) in the lower troposphere and a positive temperature anomaly in the upper troposphere. These conditions, combined with near-saturation beneath stratiform rainfall, are argued by Bister and Emanuel (1997) to favor weak downdrafts. Raymond and Sessions (2007) and Raymond et al. (2011) further argue that such a structure leads to a lower detrainment level and stronger inflow (convergence) in the lower troposphere, which in turn favors greater vorticity spinup in the lower troposphere. An additional condition of near saturation (relative humidity of at least 90%) to at least the 300-hPa level was noted by Nolan (2007) to occur immediately prior to genesis or rapid intensification.

Within the mesoscale (or subsynoptic-scale) vortex that is a fixture in all the above theories of genesis is the organization of deep moist convection. This is often represented in convective bursts that are tens of kilometers in scale, denoted “extreme convection” by Gray (1998) or vortical hot towers (VHTs) by Hendricks et al. (2004) and Montgomery et al. (2006). A central question is whether the role of deep convection is essentially stochastic (Ooyama 1982) or strongly “guided” by larger scales. D09 make the argument that meso-alpha-scale recirculation regions (“pouches”) create environments within which the statistics of the convection are predisposed to a well-defined end state where convection becomes concentrated near (i.e., within roughly 100 km of) the intersection of the disturbance critical line with the axis of the wave trough. This location, which can vary with height, is known as the “sweet spot.”

From a Lagrangian flow perspective, the sweet spot acts like an attractor, the point about which air parcels repeatedly swirl. The framework provides the concept of a dynamically isolated recirculation region in which moisture remains sufficient for deep convection to organize without convective downdrafts dominating the divergence profile. In the weakening of downdraft-induced divergence there is commonality with theories by Bister and Emanuel (1997) and Raymond et al. (1998, 2011). Furthermore, if convection were truly stochastic within the pouch, we would expect to see essentially no preferred

structure of the deep convection surrounding the sweet spot.

A central purpose of the Predepression Investigation of Cloud Systems in the Tropics (PREDICT), outlined in Montgomery et al. (2012, hereafter M12), is to determine whether the framework provided by the marsupial paradigm can lead to useful insight into the process of tropical cyclone formation and offer conceptual (and operational) tools to enhance its prediction. PREDICT was designed to follow a given system for many days consecutively or even sample a system twice in one day. Collaboration with the National Aeronautics and Space Administration (NASA) Genesis and Rapid Intensification Processes (GRIP) experiment and the National Oceanic and Atmospheric Administration (NOAA) Intensify Forecast Experiment (IFEX) was also an important part of maximizing the frequency of sampling candidate disturbances up to and beyond the point of genesis. In PREDICT, the National Science Foundation (NSF)–National Center for Atmospheric Research (NCAR) Gulfstream V (GV) aircraft deployed dropsondes to sample the atmosphere both inside and outside the recirculation region using flight plans that covered a typically rectangular region 500–800 km on a side (M12). Various satellite-derived products were crucial for real-time guidance of the aircraft; these will be used extensively to document convection organization in the present paper.

As detailed in M12, PREDICT sampled eight disturbances in 25 missions, with several flights into three cases: ex-Gaston (2–7 September) after it decayed from a tropical storm, pre-Karl (10–14 September) during its formation, and pre-Matthew (20–22 September) and Tropical Storm (TS) Matthew (24 September), a system that developed more rapidly than Karl. Analysis of the three cases, referred to as Gaston, Karl, and Matthew regardless of their stage of development, will constitute the basis of the present paper, which is intended as a side-by-side comparison of the mesoscale structure and evolution over many days either leading to genesis (Karl and Matthew) or dissipation (Gaston). Documentation of the changes in circulation, temperature, and moisture either leading up to genesis or continued weakening will allow an evaluation of some of the aforementioned theories of genesis.

Detailed summaries of these three storms are available from the National Hurricane Center (NHC) Tropical Cyclone Reports (see <http://www.nhc.noaa.gov/2010atlan.shtml>). A microwave-channel satellite summary of the three cases is presented in Fig. 1. The images<sup>3</sup> were mostly from the NASA Tropical Rainfall Measuring Mission

<sup>2</sup> The term “middle troposphere” herein refers to the layer extending roughly from 600 to 400 hPa.

<sup>3</sup> Courtesy of Naval Research Laboratory, Monterey, California.

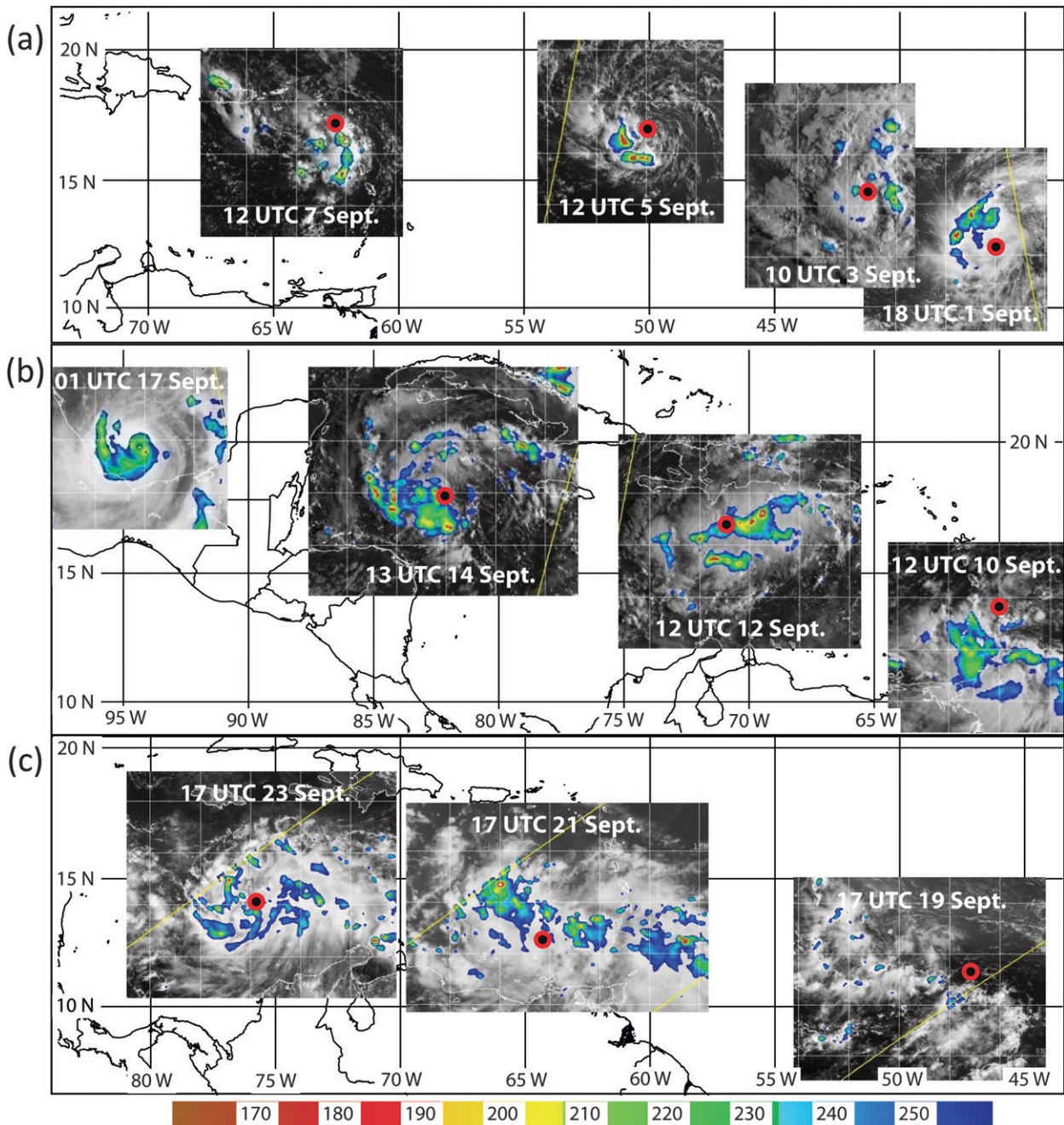


FIG. 1. Microwave images of polarized corrected temperature (K) from the Tropical Rainfall Measuring Mission (TRMM) and the Special Sensor Microwave Imager (SSM/I) superposed on visible and infrared geostationary satellite images for various times during life cycles of (a) Gaston, (b) Karl, and (c) Matthew, courtesy of the Naval Research Laboratory. The red circle with black center denotes consensus circulation center location (not shown for Hurricane Karl on 17 Sep.).

(TRMM) Microwave Imager (TMI), but a few were from the Advanced Microwave Scanning Radiometer–Earth Observing Satellite (AMSR-E) 91-GHz channel. Gaston formed in the eastern Atlantic from an African easterly wave and attained tropical storm intensity only briefly on 1–2 September. Following weakening to a remnant low it

tracked westward over the next 6 days without redeveloping into a tropical cyclone. Because the NHC outlooks placed a rather high probability (70%) on the redevelopment of Gaston for a day or so following its weakening from TS status, this case can arguably be classified as a failed genesis. The emphasis of our analysis of Gaston is

to determine why it did not reintensify on or after 2 September. Karl formed from a broad circulation that initiated near the coast of South America on 9 September and moved westward through the Caribbean. Karl became a tropical cyclone at 1800 UTC 14 September and a major hurricane in the Bay of Campeche on 17 September. Matthew formed slightly farther south and east than did Karl and its initial circulation was detectable farther east in the Atlantic than Karl's, but deep convection did not begin until 19 September (Fig. 1c). From the time of first organized convection associated with Matthew, the system reached tropical cyclone strength in just over four days, compared with five for Karl.

## 2. Data and analysis methods

Three primary sources of observations are utilized in this study: geostationary satellite data, dropsondes, and global operational analyses from the National Centers for Environmental Prediction (NCEP) and the European Centre for Medium-Range Weather Forecasts (ECMWF). Geostationary satellite observations of infrared (IR) brightness temperature, converted to temperature and archived at the Cooperative Institute for Meteorological Satellite Studies (CIMSS) were used to provide nearly continuous, half-hourly satellite coverage throughout the period of interest for each case.

Herein, we construct time–radius diagrams of IR temperature in which data are assigned to rings of width 20 km centered on the time-interpolated location of the pouch center (sweet spot). The position at 0000 UTC is defined as the average of sweet spot locations obtained from analyses provided by four operational centers (M12)<sup>4</sup> and linearly interpolated to other times. This definition of center location applies only to analyses of satellite-derived fields, not to dropsonde analyses (see below). Within each ring, there is a distribution of temperature from which a summary statistic is computed. The distribution is sometimes bimodal, especially with a combination of cirrus canopies and clear regions. Rather than rely on a parametric representation of the distribution, we use percentiles. Here we choose the 75th percentile of temperature because it represents well the radial extent of the cold cloud shield. Thus, 75% of the data in a given ring have temperatures below this value. Hovmöller diagrams are then constructed using the 75th percentile within each radial ring at each time.

To emphasize the spatial structure of precipitation, we construct maps of accumulated precipitation in the

comoving frame, computed using the Climate Prediction Center morphing technique (CMORPH) precipitation-rate analysis. Available on a 25-km grid every 3 h, these precipitation rates combine a variety of satellite observations over oceanic regions (Joyce et al. 2004). The 24-h accumulated precipitation is computed from the rain rates ( $\text{mm h}^{-1}$ ) averaged from 0300 to 0000 UTC the following day, multiplied by 24 h. An analogous depiction of convective activity is the fraction of time within a 24-h period, using half-hourly data in the comoving frame of reference, that a grid box 10 km on a side exhibits an IR temperature less than  $-60^\circ\text{C}$ . There may be numerous IR pixels that fall into one grid box, but only one value below the threshold temperature is necessary to record a count in that box. Full time resolution (30 min) is used for IR data.

From the GV, DC-8, G-IV, and P-3 aircraft dropsondes were deployed with a spacing of about 150 km, sometimes less in cases with a stronger circulation. Prior to analysis, all dropsonde data are subjected to quality control using the Atmospheric Sounding Processing Environment (ASPEN) software system. In addition, the data are visually scrutinized and a time–space correction of the drop locations is specified using translation speeds derived from the set of consensus center locations at 0000 UTC. Dropsondes from multiple aircraft are combined if deployed within 4.5 h of a chosen analysis time. The spatial location of the dropsonde data at all levels is assigned to the location at 700 hPa, hence lateral drift is ignored, but in the weak systems studied herein this amounts to only a few kilometers at most between the levels of 500 hPa and the surface.

We refine the model-derived consensus center position by computing a circulation center from the dropsonde data separately on pressure levels beginning at 1000 hPa up to 500 hPa with a spacing of 50 hPa. The circulation center is the location about which a weighted-average tangential wind, computed from observations within a  $3^\circ$  radius, is maximized (Fig. 2). The  $3^\circ$  radius is chosen to include enough dropsondes from each mission for a meaningful average (typically 10 or more) yet still remained confined within the nascent cyclonic circulation. A weighted average is used to compensate for unevenness in the spatial distribution of observations about a candidate center location. Tangential winds from all observations within a given quadrant are averaged first, and then the average of the four quadrants is computed to obtain the average tangential wind (Davis and Trier 2007). Quadrants are defined according to cardinal directions—that is, from due east to due north of the center (quadrant 1), due north to due west (quadrant 2), and so on. The average tangential wind  $V_T$  varies with pressure only.

Once the location of the center is computed at each level, the average tangential wind serves as a measure of

---

<sup>4</sup> The operational centers were NCEP, ECMWF, the UK Met Office, and the U.S. Navy.

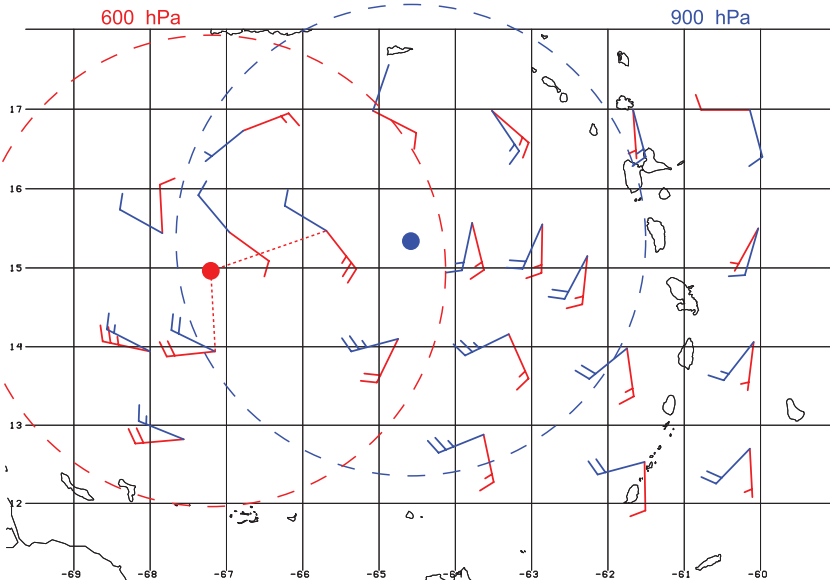


FIG. 2. Example showing results of applying center-finding algorithm (described in text) on two pressure levels, 900 hPa (blue wind symbols) and 600 hPa (red) valid at 1800 UTC 11 Sep, prior to the formation of Karl. Filled circles indicate center locations at each level. Dashed circles indicate  $3^\circ$  radius from each center. The example here shows centers at these two altitudes displaced by nearly 300 km.

the intensity of the disturbance at that level. Vertical profiles of  $V_T$  at successive times depict whether intensity grows upward or downward, and how rapidly the overall intensity changes. The differences in locations of centers at different altitudes indicate the “tilt” of a system with height, although it may be more appropriate to think of large displacements as misalignments.

There is clearly some potential for sensitivity of the computed center location to measurement errors, sampling errors, and errors in estimating the speed of the comoving reference frame. The influence of measurement and representativeness errors is crudely assessed by assigning random wind errors to the observations with a white noise spectrum bounded at  $\pm 2 \text{ m s}^{-1}$ . The assumed magnitude of errors is somewhat ad hoc, and therefore the error analysis is more appropriate for assessing relative uncertainty than absolute uncertainty. The center location is recomputed 100 times with the perturbed observations, and the standard deviation of center locations provide a time- and level-dependent estimate of position uncertainty (section 4). Possible errors in the translation speed are assessed separately by simply applying offsets to the zonal speed as large as  $\pm 2 \text{ m s}^{-1}$ . In general, the center location is not sensitive to these variations in the assumed system translation speed.

Area mean radial wind is computed analogously to the mean tangential wind. Given a center location (herein at

900 hPa), the radial wind within  $3^\circ$  from the center is first averaged within quadrants, and then the mean radial wind is computed from the quadrant averages. The mean divergence over a circle of radius  $R$  is  $2\bar{u}_R/R$ , where  $\bar{u}_R$  is the azimuthally averaged wind at radius  $R$ . We use the mean radial wind and the mean radial distance of the observations from the center to estimate divergence from this expression. The divergence is integrated vertically to obtain profiles of  $\omega = dp/dt$  assuming  $\omega = 0$  at 1025 hPa with a vertical increment of 50 hPa, hence staggered with respect to divergence. System-relative flow and vertical wind shear are also computed using quadrant averages of the vector wind and vector wind difference between two layers, respectively.

The uncertainty in divergence and vertical motion is assessed using the same random perturbations to winds that were used to assess the uncertainty in circulation center location. However, uncertainty (error) in vertical motion requires an assumption about the vertical correlation of errors. Herein we compute two scenarios: uncorrelated and perfectly correlated. While the error in vertical motion grows with height in both cases, it grows roughly 3 times faster when errors are correlated. Errors also vary substantially from mission to mission, as discussed in section 4e.

In general, the objective analysis or gridding of the dropsonde data is not performed. However, to obtain a synoptic-scale perspective in section 4c, the dropsonde

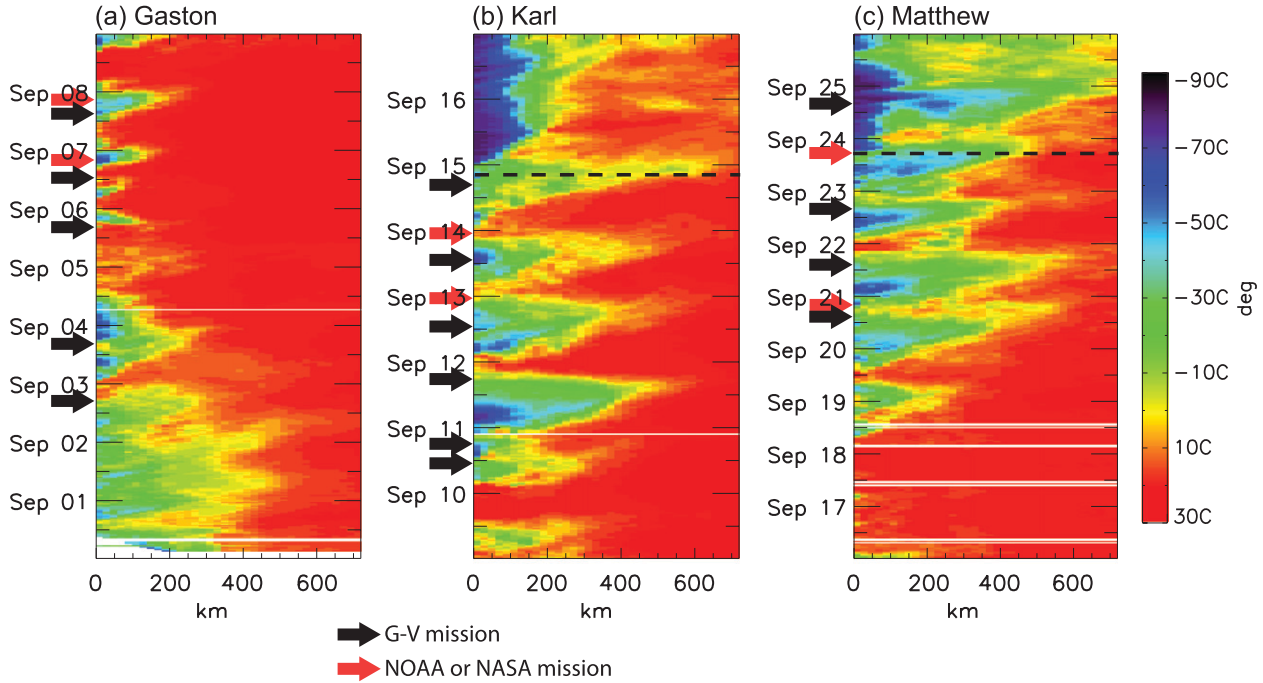


FIG. 3. Time–radius diagrams of cloud-top temperature derived from Geostationary Operational Environmental Satellite (GOES) IR data, where the 75th percentile temperature within each radial ring of 20-km width is plotted. Arrows indicate when dropsonde missions occurred (black for GV, red for NOAA or NASA). Dashed lines denote time of tropical storm formation for Karl and Matthew.

and GFS relative humidity (outside a  $3^{\circ}$  radius from the model consensus circulation center) are analyzed together using an objective analysis scheme based on Delaunay triangulation that is available from Interactive Data Language (IDL) software.

### 3. Satellite observations

#### a. Time dependence

Time–radius diagrams of the 75th percentile of IR temperature are shown in Fig. 3 for each of the three cases studied herein. As may be expected, the three cases exhibit markedly different behavior over the course of the 8–9 days that are presented. Cloud tops early in the evolution of Gaston, both during its genesis on 1 September and as a weak tropical storm, are mainly in the range of  $-30^{\circ}$  to  $-40^{\circ}\text{C}$  near the circulation center. Beginning around the time of the second GV mission into Gaston, convection almost completely dissipates. A strong burst of convection occurs on 4 September, but after that deep convection is relatively short-lived and the associated cold clouds extend barely to 200 km from the center. Long periods of little convective activity are apparent, whereas a clear diurnal signal is not obvious until perhaps 6 September.

The Hovmöller diagrams for Karl and Matthew feature larger bursts of convection than seen for ex-Gaston,

with the radial extent of the cold cloud approaching 600 km. After progressing steadily outward, the cold cloud signature dissipates nearly simultaneously at all radii. The bursts of convection in Karl and Matthew retain an approximately diurnal variation in which the initiation of the cold cloud signature begins between 1200 and 1500 UTC on most days. While the tropical maritime convective maximum is generally known to occur in the early morning (Yang and Slingo 2001), the diurnal peak in the Caribbean was found by Sorooshian et al. (2002) and Hirose et al. (2008) to occur as late as midday. This timing is consistent with the convective maxima in all three cases studied herein during the periods when these disturbances were over the Caribbean Sea. In Karl and Matthew, genesis marks the transition from diurnally dominated convection fluctuations to a relatively constant presence of a cold cloud shield.

The time dependence of the deep convection is emphasized in Fig. 4, which shows the fractional area covered by cloud tops colder than  $-60^{\circ}\text{C}$  within 200 km of the model-consensus center location. Also shown are the median and 95th percentiles of rain rates within the same area derived from CMORPH data. These time series show the strongly pulsating nature of the convection, more regular and with larger median rain rates and more prevalent cold cloud tops for Karl and Matthew than for Gaston. The 95th percentile rain rates do not differ markedly for

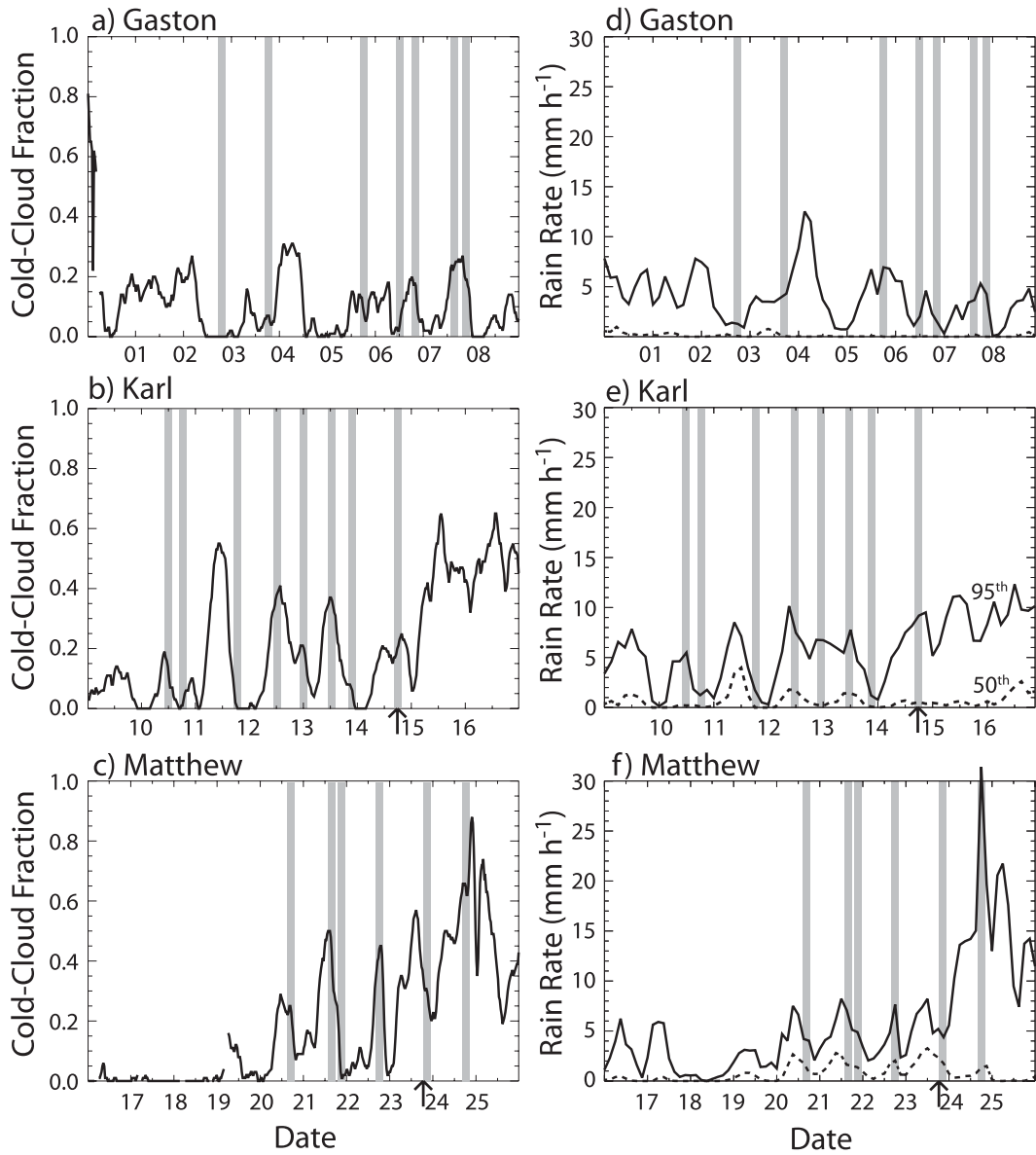


FIG. 4. Time series of (left) fractional coverage of cloud tops of  $-60^{\circ}\text{C}$  or colder within 200 km of the circulation center and (right) the 95th and 50th percentiles of the CMORPH rain rate ( $\text{mm h}^{-1}$ ) distribution within 200 km of the center, for (top) Gaston, (middle) Karl, and (bottom) Matthew. Gray bars are times when dropsonde missions were conducted (approximate duration).

Gaston versus Karl and Matthew until the latter portion of the time series. The implication is that Gaston maintained some intense convection throughout its life cycle, but that convection covered a much smaller area than in developing cases.

#### *b. Evolution of precipitation patterns*

##### 1) GASTON

Using the CMORPH data as described in section 2, we construct composite images of time-space-corrected,

system-relative winds and precipitation accumulated over 24 h in the comoving frame. One image per day indicates the characteristic spatial structure of precipitation within the disturbance. Winds at 700 hPa are used as an indication of the circulation in the lower midtroposphere.

Gaston exhibits a clear separation of the remnant tropical storm and the intertropical convergence zone (ITCZ) on 2–3 September (Figs. 5a,b). Rainfall is concentrated slightly northwestward from the center of circulation on both days. By 5 September, the area of 24-h rainfall greater than 8 mm has shrunk considerably, although heavier

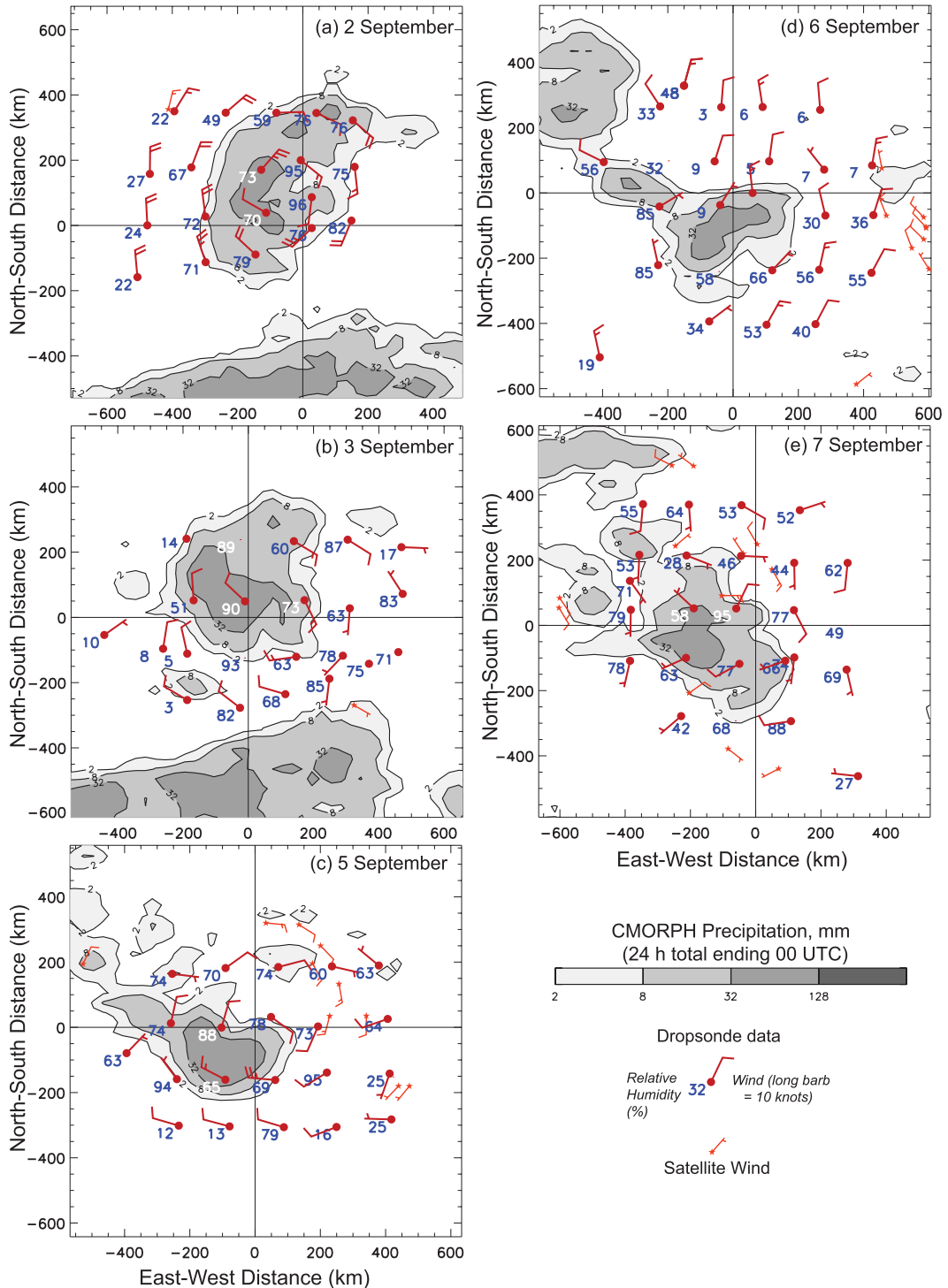


FIG. 5. CMORPH 24-h accumulations for each day (see text for details) and 700-hPa system-relative wind in the comoving frame, with 700-hPa relative humidity for Gaston. Locations of observations are time-space-corrected, valid at (a) 1800 UTC 2 Sep, (b) 1800 UTC 3 Sep, (c) 1800 UTC 5 Sep, (d) 1500 UTC 6 Sep, and (e) 1500 UTC 7 Sep.

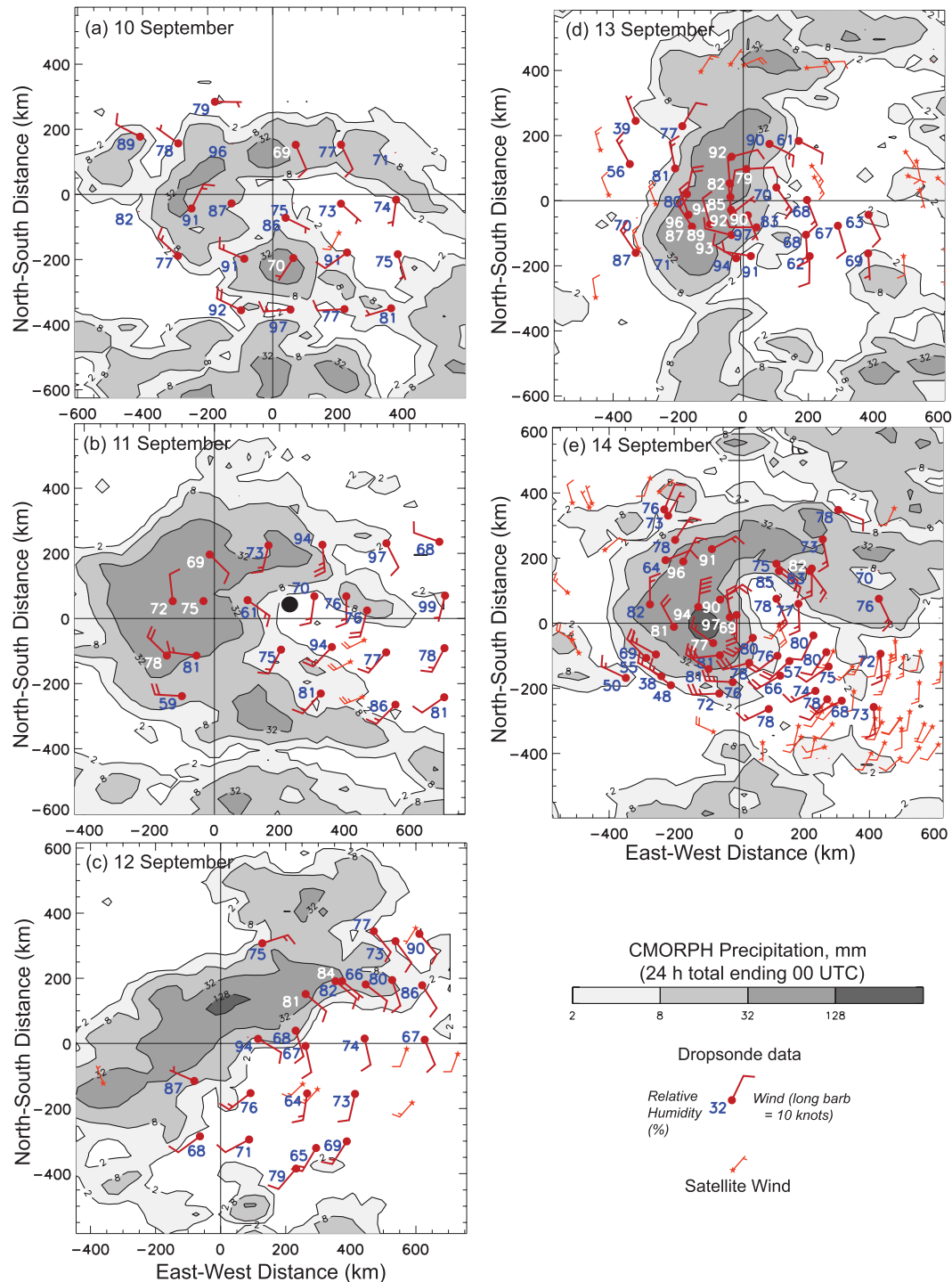


FIG. 6. As in Fig. 5, but for Karl. Locations of observations are time–space corrected, valid at (a) 1200 UTC 10 Sep, (b) 1800 UTC 11 Sep, (c) 1200 UTC 12 Sep, (d) 1200 UTC 13 Sep, and (e) 1800 UTC 14 Sep. Note that in (b), the easternmost line of dropsondes has been omitted (see Fig. 10a). Data in (d) and (e) represent data combined from NSF, NOAA, and NASA aircraft.

rainfall is still evident near and slightly southwest of the comoving circulation center. The ITCZ is no longer seen in the domain. The circulation has clearly weakened further, and it continues to do so during the ensuing day so that by 6 September the circulation at 700 hPa is poorly defined. Convection near the center of the comoving circulation is still apparent even though very dry air (humidity less than 20%) can be found less than 300 km away. The presence of widespread dry air is a defining characteristic of the environment surrounding Gaston. A detailed analysis of the origin of this dry air is not attempted herein.

## 2) KARL

During the first mission into pre-Karl, centered on 1200 UTC 10 September, precipitation features an arced band to the north of the weak circulation center at 700 hPa (Fig. 6a). Precipitation is more extensive spatially about the center than for Gaston even when Gaston maintained a stronger circulation. There is a suggestion of an east–west zone of convection roughly 500 km to the south of the circulation center, which is probably related to convection over South America.

On the following day (Fig. 6b), rainfall exceeding 8 and 32 mm has become markedly more widespread. An arced band north of the circulation center is still apparent, but significant rainfall exists near the center of cyclonic circulation at 700 hPa. By 12 September (Fig. 6c), rainfall has aligned along a southwest–northeast axis and the maximum rainfall has increased to more than 128 mm. Convection within this region combined with air space restrictions made it difficult to sample the northwest side of the circulation. It appears that most of the heavy rainfall was located to the northwest of the 700-hPa circulation center (in the comoving frame).

By 13 September (Fig. 6d), the heavy rainfall (more than 32 mm) has consolidated somewhat and become oriented more along a north–south axis centered about 100 km to the west of the circulation center. Further consolidation occurs on 14 September (Fig. 6e), with heavy rainfall very near, perhaps slightly to the west, of the circulation center. To the north, the arced band of rainfall has reemerged. The precipitation distribution near the time of genesis of Karl looks similar (although more widespread and intense) to the distribution during the first flight into Gaston, which occurred when it was near tropical storm strength.

On 10–11 September, the relative humidity at 700 hPa averages roughly 80% with little obvious mesoscale organization. By 13 September, the relative humidity is greater on the west and northwest side of the circulation in association with the location of greater rainfall. Humidity values on the eastern and southern side of the circulation are generally around 70% (60%–80%), although

some even drier air is apparent on the southwestern periphery on 14 September.

## 3) MATTHEW

The precipitation pattern during the early development of Matthew (Fig. 7) is generally less structured than for Karl. In general, the heavier rainfall is elongated along an east–west axis, as is the cyclonic circulation. The cyclonic circulation was well sampled by dropsondes on 22 September when the average precipitation hints of some consolidation slightly to the east of the circulation center but also a reduction in the area covered by rainfall greater than 32 mm. Heavier rainfall is further concentrated near the center on 23 September close to the time of genesis, and a large region of rainfall exceeding 128 mm is apparent on 24 September when Matthew is a moderate tropical storm. It is also of interest that the spatial pattern of precipitation in the comoving frame on 24 September strongly resembles that for Karl (at multiple times) and Gaston on 2–3 September.

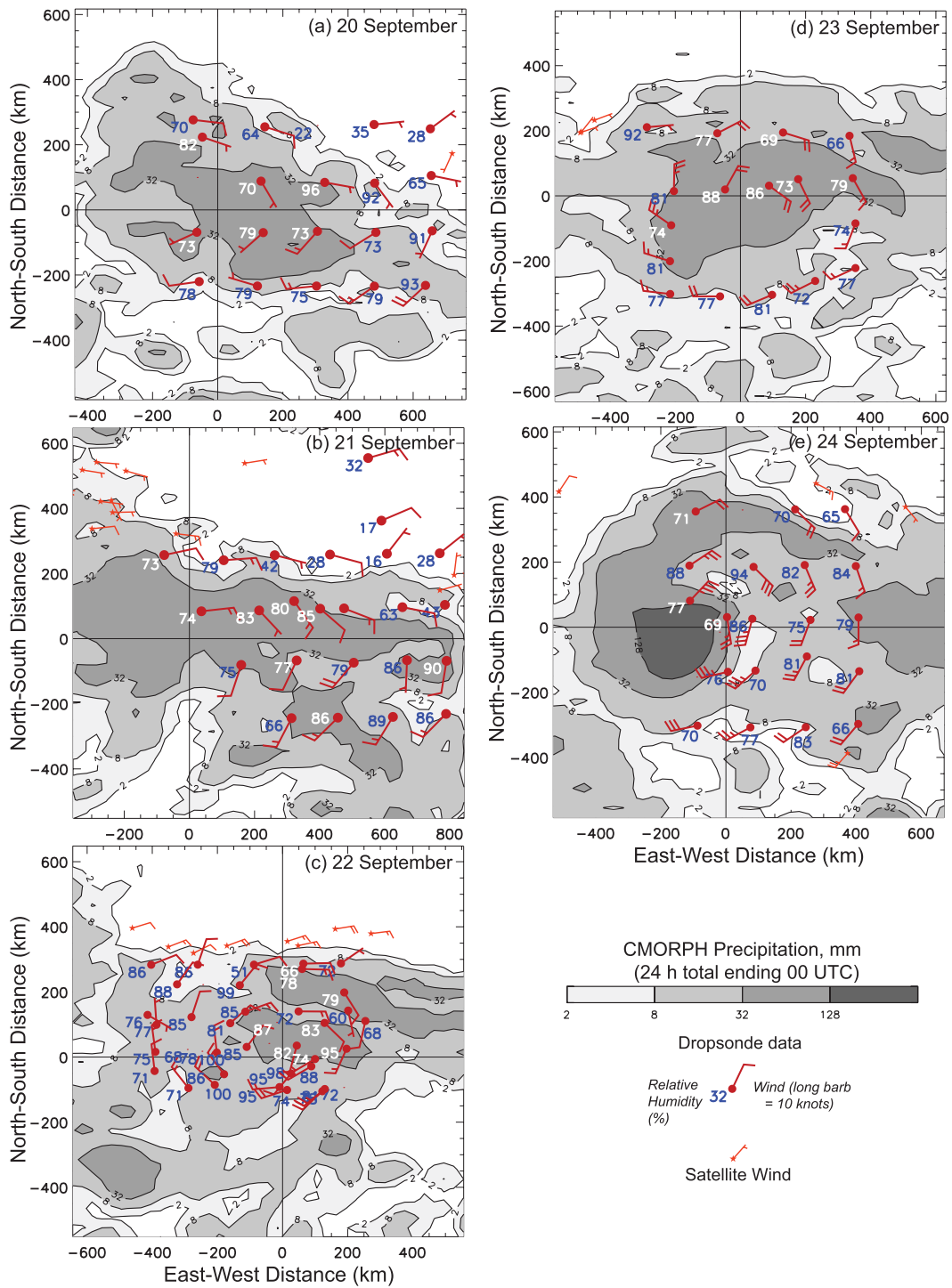
The relative humidity is rather uniform over the region of cyclonic circulation with an average of 75%–80%. However, higher relative humidity is evident near the circulation center on 22 and 23 September, with values on 22 September near 100%. By contrast, marked dryness appears to the north of the rainfall region with relative humidity observed to be near 30% or less on 20 and 21 September.

## 4. Dropsonde data analysis

### a. Circulation

With the numerous research missions that occurred in each of the three systems, it is possible for the first time to document the temporal evolution of the vertical profile of circulation in detail for both developing and decaying cases. One profile is constructed for each mission by computing the maximum average tangential wind separately at each pressure level. Thus, the profiles are not generally vertical profiles of circulation about a fixed location, but rather the profile of the strongest circulation at each level. While the average tangential wind is not precisely related to the area-averaged vorticity (and hence the true definition of circulation), we refer to the average of the tangential wind as circulation herein.

In general, the largest systematic changes in circulation occur between 700 and 500 hPa (Fig. 8), with increases for Karl and Matthew prior to genesis, and a decrease for Gaston. Gaston weakens markedly at these levels before its strength within the lowest 200 hPa diminishes substantially. Karl exhibits a well-defined vortex in the lowest 200 hPa even at the time of the first mission when it is



still quite weak in the middle troposphere. The circulation near the surface actually decreases by 13 September. Near 800 hPa, the circulation changes little over four days and only increases rapidly near the time of genesis.

Matthew exhibits more of a vertically uniform increase of circulation at all levels; however, the circulation increases more rapidly at 600 hPa than below 800 hPa through 22 September, one day prior to genesis.

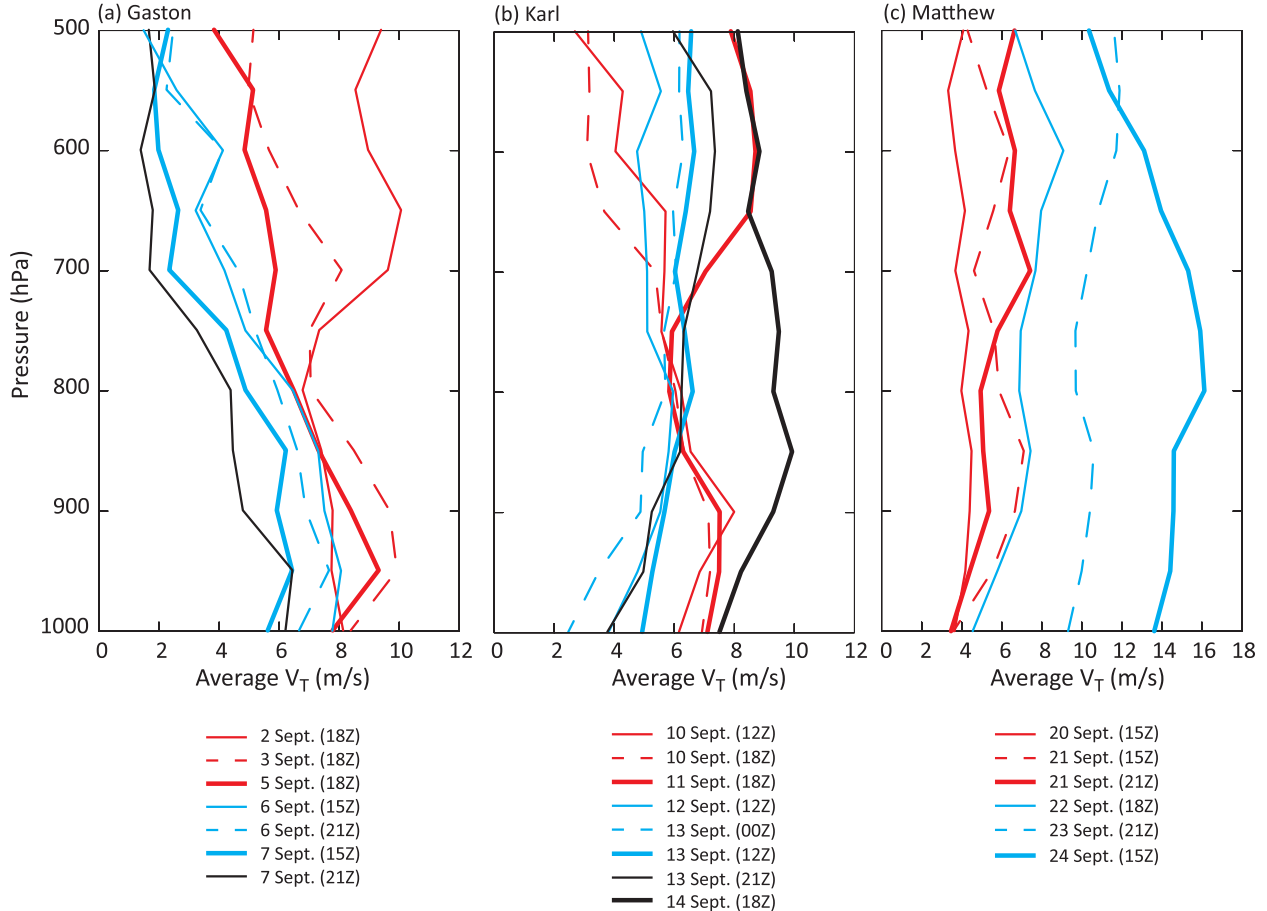


FIG. 8. Profiles of average tangential wind ( $\text{m s}^{-1}$ ) representing the maximum circulation at each pressure level (spaced at a 50-hPa interval). Note that circulation centers at different altitudes need not be collocated. See color legend below each plot; one profile per mission.

The spatial relation of circulation centers at different altitudes varies considerably over time. This is illustrated using the position of the centers at 900 and 500 hPa derived from each mission, along with the uncertainty estimate of the center location (Fig. 9). Where the two circles overlap at a given time, there is no misalignment that can be identified within the limitations of the data, using a random error constrained within  $\pm 2 \text{ m s}^{-1}$ .

For Gaston, the midtropospheric vortex is initially displaced poleward of the low-level vortex, but the midtropospheric vortex moves equatorward in a relative sense as it weakens. By 6 September, the midtropospheric vortex has weakened markedly, and the original center can no longer be clearly identified. No well-defined circulation center exists at 500 hPa on or after 6 September. It is only up to about 700 hPa that the original vortex associated with Gaston is traceable for the entire 5 days (Fig. 5).

Karl maintains a large displacement between its low-level and midlevel circulation centers until 13 September (i.e., one day prior to genesis; Fig. 9b). On 10 September, the weakness of the midlevel circulation leads to considerable

uncertainty in the displacement, but it appears to be generally equatorward relative to the low-level center. A pronounced and unambiguous misalignment appears on 11 September in conjunction with the major convective burst that forms a new center at the midtroposphere to the west of the low-level center (see also Figs. 2 and 6). This misalignment shrinks over time and the midlevel center migrates to a position slightly equatorward of the low-level center by late on 13 September.

In the early stages of its existence, Matthew is weak at all levels and exhibits both apparent misalignment and also considerable uncertainty regarding the location of the circulation (Fig. 9c). Some of the misalignment and uncertainty may arise from the asymmetric sampling of the circulation on 21 September due to air space restrictions. Beginning on 22 September, Matthew exhibits minimal misalignment until after genesis, although there is some uncertainty. The tilt, or misalignment, that develops after Matthew achieves tropical storm strength may be indicative of vertical shear (see below) that limited Matthew's maximum intensity.

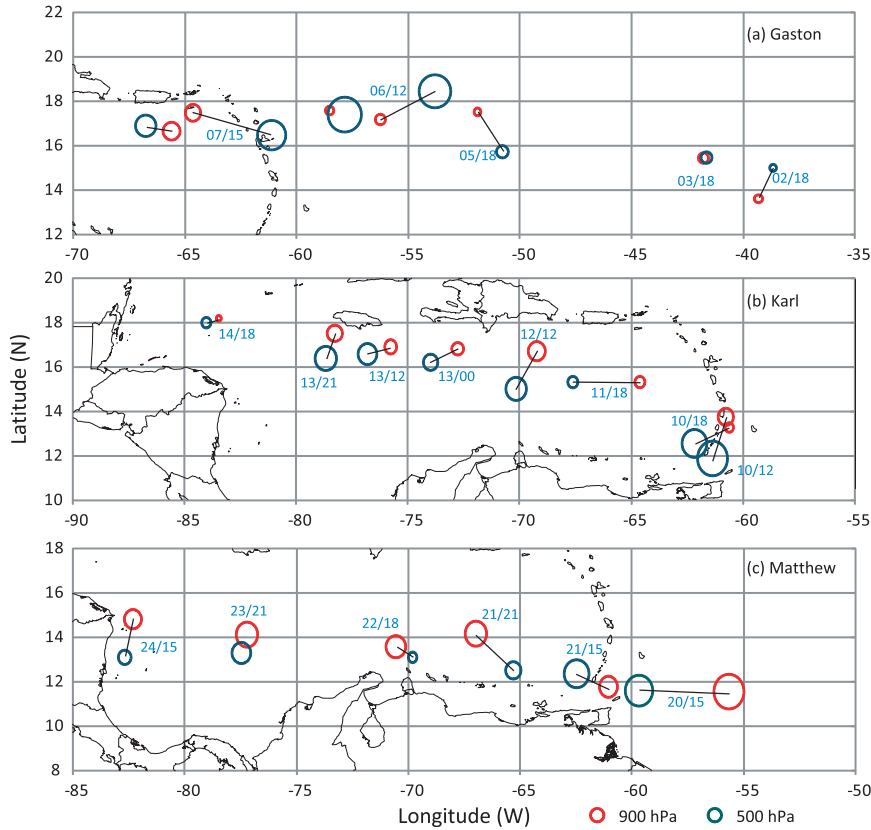


FIG. 9. Positions of 900- (red) and 500-hPa (blue) circulation centers, where size of circle represents the spatial standard deviation of the perturbed observations sample. Thin lines connect centers that are statistically distinct in position. Labels in blue indicate the date of September/hour (UTC).

### b. Vertical shear and relative flow

The vertical shear is computed as the vector wind difference between 925 and 500 hPa (Fig. 10). Two estimates of vertical shear are computed: the “environmental shear,” which acts on the vortex to induce asymmetries (such as vortex tilt), and the total shear, which partly results from asymmetries of the vortex and can influence the flow of air into the circulation from the environment. The layer chosen tends to encompass the depth of predepression circulations and is therefore more representative of shear effects than would be a layer extending to 200 hPa.

The environmental shear is derived from regional subsets of global analyses by solving a Poisson equation for the streamfunction and velocity potential associated with vorticity and divergence, respectively, within  $5^\circ$  of the circulation center<sup>5</sup> at the top and bottom levels of

the shear layer. The nondivergent and irrotational winds so derived are subtracted from the full winds, and the resultant winds are used to compute the shear without the disturbance (Davis et al. 2008). The same procedure is applied to both NCEP and ECMWF analyses. The environmental shear values derived from the two analyses are generally in good agreement (Fig. 10). In Fig. 10, and in other time series, we denote arbitrarily 0000 UTC on the day of the first mission as  $t = 0$ . According to this definition, Karl becomes a tropical storm at  $t = 114$  h and Matthew at  $t = 90$  h.

The total shear derived from the dropsondes (section 2), which includes the contribution from the disturbance itself, is often larger than the environmental shear (Fig. 10). For Gaston, except for a brief period on 3 September, the total shear is notably larger than the background shear, and both increase from 3 to 6 September. This result suggests that while the environmental shear is generally small until at least 5 September, the misalignment of the vortex (see Fig. 9) creates localized shear that will affect moisture transport and the response of convection. Most

<sup>5</sup> For the analysis-derived shear, the consensus center is used. But since the disturbance is removed, the shear is not sensitive to the exact location chosen as the center.

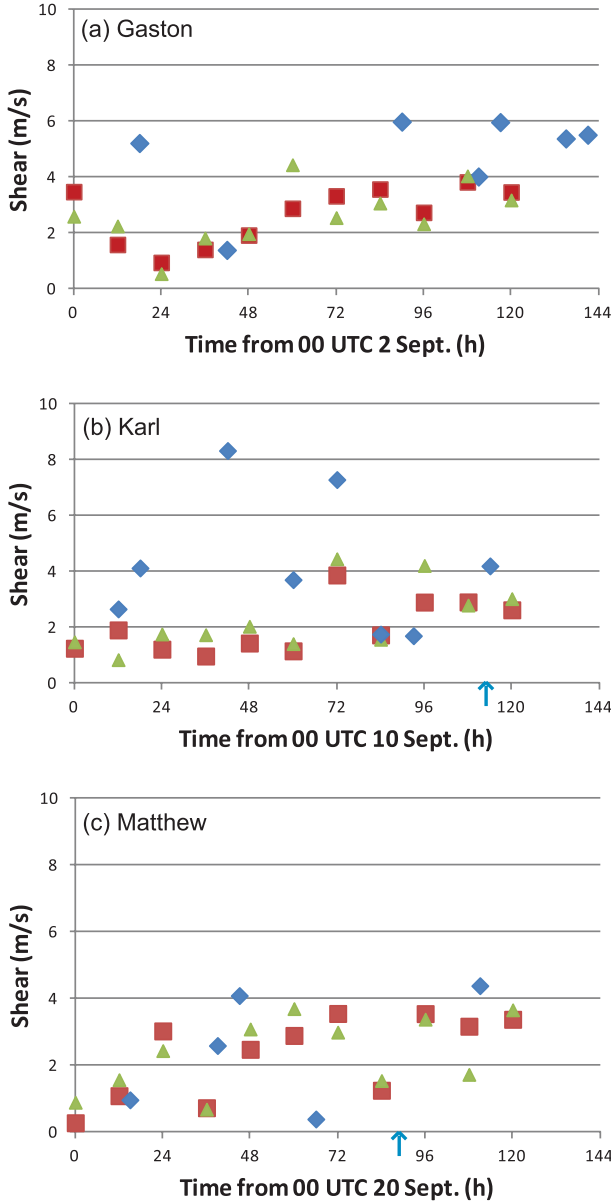


FIG. 10. Vertical shear from 925 to 500 hPa ( $\text{m s}^{-1}$ ). GFS (maroon squares) is the Global Forecast System operational analysis ( $1^\circ$  grid), EC (green triangles) is the ECMWF operational analysis ( $0.25^\circ$  grid), and Obs (blue diamonds) refers to dropsondes within a  $3^\circ$  radius of the center at 900 hPa. Background shears are defined in text. Blue arrows on abscissa denote time of tropical storm formation for Karl and Matthew.

of the pregenesis period of Karl until 13 September features large total shear<sup>6</sup> yet small background shear, again consistent with the misalignment of mid- and

<sup>6</sup> Recall that the layer over which shear is defined is only about 5 km deep, compared with more conventional definitions of vertical shear in the 850–200-hPa layer, which is over 10 km deep.

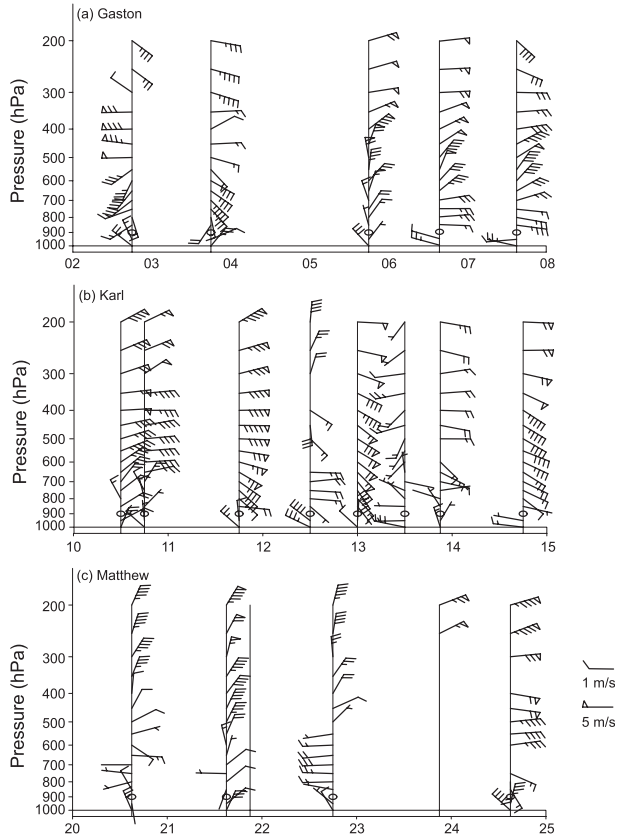


FIG. 11. Profiles of relative flow averaged within  $3^\circ$  of 900-hPa circulation center. Note scale for wind barbs at lower right. Profiles at 2100 UTC 6, 7, and 21 Sep are omitted for clarity. Missing relative winds on 23 Sep result from observations absent from one quadrant.

lower-tropospheric circulations (Fig. 9). For Matthew the situation is reversed: the shear prior to genesis remains weak but increases slightly near and after genesis.

Profiles of system-relative flow (Fig. 11), computed from dropsonde data with respect to the 900-hPa circulation center (section 2), include the influence of the disturbance itself. Deep westerly flow in Gaston on 2 September (Fig. 11a) is consistent with the northward or northeastward tilt of the vortex with height (Fig. 9). Flow around the misaligned midtropospheric circulation center produces westerlies above the 900-hPa center. The pattern approximately reverses by 5 September, implying a southward tilt with height, and the midtropospheric relative flow strengthens from the northeast to at least  $5 \text{ m s}^{-1}$  and remains so through 7 September.

Relative flow profiles for Karl reveal easterly and southeasterly relative flow above 900 hPa until 1200 UTC 13 September (Fig. 11b). Some of this flow is attributable to the environmental shear (Fig. 10) but some results from the midtropospheric circulation being displaced to the west or southwest of the lower-tropospheric circulation. Profiles at 1200 and 2100 UTC 13 September show weak relative

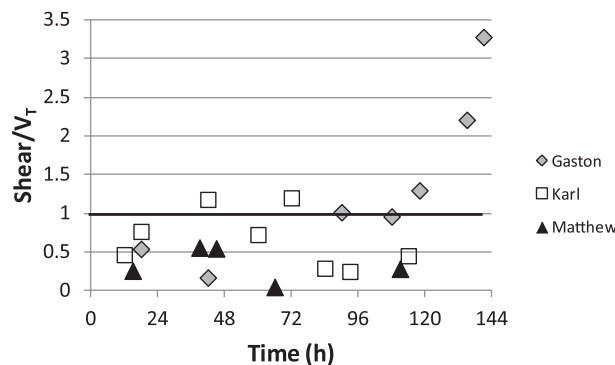


FIG. 12. Vertical shear (total shear as in Fig. 11) normalized by average tangential wind at 700 hPa. The latter is computed relative to 700-hPa circulation center.

flow that is consistent with the near-vertical alignment of the circulation centers at these times (Fig. 9b). The relative flow prior to the genesis of Matthew is small compared to that in the other two cases, especially in the layer from 900 to 500 hPa (Fig. 12c). However, after genesis late on 23 September, relative flow and vertical wind shear increase.

A summary of the vertical shear in each of the three cases is depicted in Fig. 12 as total shear normalized by the strength of the circulation at 700 hPa (near the middle of the shear layer). The normalization accounts for two factors. First, the resiliency of vortices in shear depends on the vortex strength (in adiabatic conditions). Stronger vortices will precess more readily and mitigate the effect of shear (Reasor et al. 2004). Second, the relative trajectories of the flow—in particular, the point of closest approach of environmental air to the circulation center—will depend on this ratio (Riemer and Montgomery 2010). The normalized shear is strong (near or greater than unity) over a 2-day period prior to the formation of Karl. It then abruptly decreases prior to genesis. The normalized shear in Matthew is near or below 0.5 throughout. By contrast, although the normalized shear for Gaston is initially low, it increases rapidly over time and becomes much greater than unity as Gaston decays. The rapid rise in normalized shear is likely as much the result of the weakening circulation as a cause of the weakening. But the decreasing resilience of the vortex and the increasing proximity and infiltration of environmental air imply an increasingly lengthened path of recovery to a condition favorable for genesis.

### c. Moisture

Vertical profiles of relative humidity averaged within  $3^{\circ}$  of the center of circulation at 900 hPa<sup>7</sup> (Fig. 13) show

that there is little time variation of relative humidity structure for Karl and Matthew, although some variability is noted near and above 600 hPa. For Gaston, the relative humidity in the middle troposphere steadily declines from 2–6 September. In all cases, the average relative humidity decreases markedly above 500 hPa despite the fact that relative humidity below  $0^{\circ}\text{C}$  is computed with respect to ice saturation.

The temporal decrease of moisture for ex-Gaston is also seen in the radial profiles of ice-saturation fraction in the 600–400-hPa layer (Fig. 14a). This is the precipitable water in the layer divided by the saturation precipitable water in the layer (with respect to ice saturation colder than  $0^{\circ}\text{C}$ ). This layer is chosen because it represents much of the spatial and temporal variability of water vapor in the column and because the occurrence of saturation in the middle troposphere has been hypothesized as important to genesis (Nolan 2007; Sippel and Zhang 2008). Within  $2^{\circ}$  of the center, saturation fraction is initially around 0.8 just after Gaston had been downgraded to a tropical depression, but there is large variability. By 6 September there are numerous values below 0.4 in the same area.

Karl features an increase in saturation fraction between 10 and 14 September, with numerous dropsondes indicating conditions near ice saturation within  $2^{\circ}$  of the circulation center by 14 September (Fig. 14b). For Matthew (Fig. 14c), there are high values of saturation fraction within 200 km of the center throughout. Dry air is located on the northeastern periphery of the circulation (not shown) but does not penetrate near the center. In all cases there is considerable variability of saturation fraction at a given radius. However, within a  $2^{\circ}$  radius, there is notably larger variability of saturation fraction in Gaston that is perhaps indicative of greater lateral mixing and more localized vertical moisture transport than in Karl or Matthew.

A central question regarding the lack of redevelopment of Gaston is how the dry air affected the inner part of the cyclonic circulation. As Fig. 15 demonstrates, consistent with Figs. 9 and 11, the misalignment of the cyclonic circulation centers at different altitudes produces strong relative flow above the lower-tropospheric circulation center. First on 2 September, when westerlies were able to transport dry air above the low-level circulation, then on 5 September, when the large-scale shear from the northeast led to a large displacement of the midtropospheric vortex, midtropospheric relative flow is clearly seen. On 5 September, the relative flow acts to transport dry air southward directly over the circulation center at 900 hPa. The result of this transport is the low humidity values on 6 September (Figs. 13 and 14).

<sup>7</sup> All thermodynamic diagnostic variables are similarly averaged. All buoyancy-related parameters are computed first from individual soundings, and then averaged.

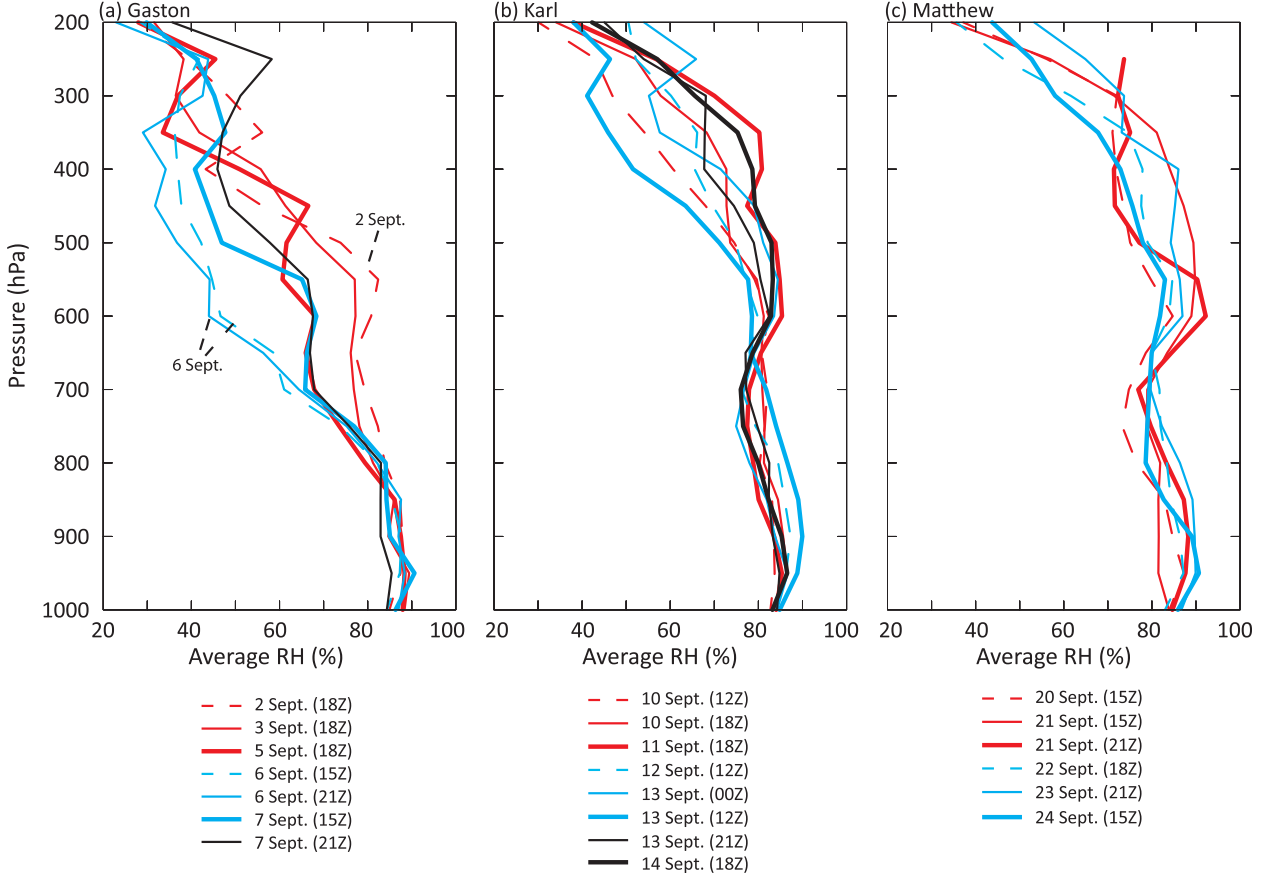


FIG. 13. Profiles of relative humidity averaged from dropsondes within  $3^{\circ}$  of circulation center at 900 hPa.

#### d. Temperature and thermodynamic stability

To isolate the virtual potential temperature perturbation of the disturbance, we subtract from the average profile within a  $3^{\circ}$  radius of the 900-hPa center a profile constructed from dropsondes within a ring extending from  $3^{\circ}$  to  $6^{\circ}$  from the center (Fig. 16). The latter is taken to represent the environment of the disturbance. A similar approach was used in Davis and Trier (2007). Using this definition, the environment of the disturbance is allowed to evolve with time.

For Gaston, there is a warm anomaly in the lower and middle troposphere<sup>8</sup> that weakens and becomes shallower with time, consistent with the trend in the cyclonic circulation. The magnitude of the warm anomaly in the lower troposphere is about  $1^{\circ}\text{C}$ . The anomaly at 400- and 500-hPa changes from positive to negative from 2 to 6 September. A weak warm anomaly exists in the upper troposphere throughout.

Karl and Matthew exhibit very different thermal anomalies from Gaston. In particular, a lower-tropospheric warm anomaly early in Karl's evolution is replaced by a negative anomaly prior to genesis. Near the surface, a slight cool anomaly exists at all times, though it is somewhat larger prior to genesis. A warm anomaly of about  $1^{\circ}\text{C}$  develops in the middle and upper troposphere; combined with cooling in the lower troposphere, this creates a positive perturbation of static stability. This is broadly consistent with the preferential increase of circulation in the middle troposphere (not shown) that arises from the combined influences of vortex vertical alignment (Fig. 9) and strengthening of the maximum midtropospheric circulation (Fig. 8). The thermal profiles for Matthew reveal a slight increase in virtual potential anomaly with height, somewhat similar to Karl. The whole troposphere warms with time within the circulation relative to its surroundings while the static stability perturbation does not change systematically.

Moist thermodynamic stability may be assessed by various metrics. Here we compute the moist static energy (MSE)  $M = C_p T + gz + L_v q_v$  and normalize it by  $C_p$  to obtain units of kelvins. From Fig. 17, showing the

<sup>8</sup> The cool anomaly centered on 800 hPa on 2 Sep appears because of particularly warm air on the northwest periphery of Gaston's circulation near this pressure level.

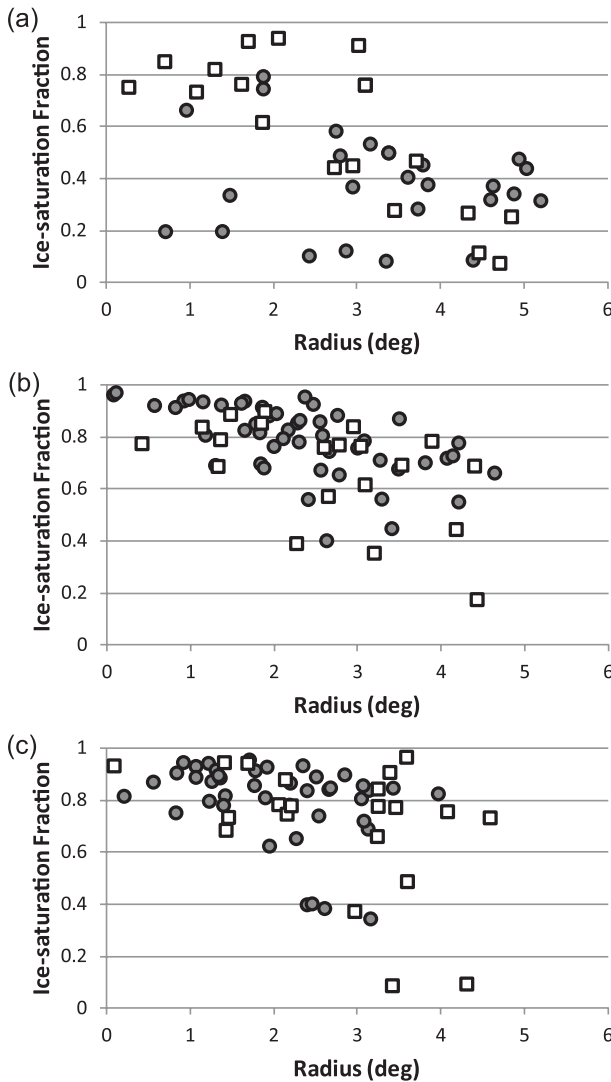


FIG. 14. Ice-saturation fraction (saturation fraction defined with respect to ice saturation) in the layer from 600 to 400 hPa as a function of radius from the circulation center at 900 hPa for (a) Gaston, (b) Karl, and (c) Matthew. Squares denote the first mission into each system [2, 10, and 20 Sep in (a), (b), and (c), respectively], and filled circles denote missions on (a) 1500 UTC 6 Sep, (b) 1800 UTC 14 Sep, and (c) 1800 UTC 22 Sep.

average MSE among dropsondes within  $3^\circ$  of the 900-hPa circulation center, it is apparent that the trends in MSE are small or slightly positive at both 950 and 500 hPa for Karl and Matthew. However, for Gaston, the boundary layer MSE increases while the midtropospheric MSE decreases. The increase in the boundary layer MSE is consistent with the observed increase of SST of about  $2^\circ\text{C}$  from 2 to 6 September and the accompanying increase of moisture (the relative humidity remains roughly constant; Fig. 13). The decrease of MSE in the middle troposphere is mainly due to drying. It also turns out that the maximum buoyancy of undilute parcels lifted

from the boundary layer of Gaston increases from about 1 K on 2 September to nearly 6 K on 7 September and occurs at 400 hPa (not shown). The maximum buoyancy of lifted parcels in Matthew and Karl is not larger than 3 K, is relatively constant in time, and occurs near 600 hPa. The greater conditional instability in Gaston compared to developing cases was also noted by Smith and Montgomery (2011, manuscript submitted to *Quart. J. Roy. Meteor. Soc.*, hereafter SM) and is consistent with theoretical concepts advanced in Raymond and Sessions (2007).

The potential for strong downdrafts is assessed using downdraft CAPE (DCAPE; Emanuel 1994; Gilmore and Wicker 1998). The DCAPE shown in Fig. 18 represents the maximum value obtained for any parcel originating below 400 hPa.<sup>9</sup> Gaston features DCAPE values that are initially only slightly larger than values for Karl and Matthew. With time, the downdraft potential within the circulation of Gaston increases, judging from the increase of DCAPE. Values for Karl and Matthew do not increase, and there is a suggestion of a decrease of DCAPE with time for Karl near the time of genesis. Note that DCAPE is never close to zero; there is always some potential for downdrafts.

#### e. Vertical motion

Profiles of vertical motion,  $\omega = dp/dt$ , averaged with  $3^\circ$  of the 900-hPa circulation center, show important variations during the life cycle of each disturbance (Fig. 19). Profiles for Matthew and Gaston are somewhat more uncertain than profiles for Karl (dashed profiles in Fig. 19), based on computations using random perturbations of wind observations outlined in section 2. For Gaston, the lower-tropospheric ascent on 2 September, the midtropospheric subsidence on 5 September, and the deep ascent on 7 September are the most robust features. Many profiles indicate weak ascent in the lower troposphere that is qualitatively consistent with frictionally induced convergence. The shallow ascent on 2 September is consistent with the small amount of buoyancy noted on that day (section 4d). Subsidence on 5 September may result from the increasing misalignment of mid- and lower-tropospheric vortex centers (Raymond and Jiang 1990). Ascent on 7 September is associated with somewhat invigorated deep convection.

In the case of Karl, the vertical motion profiles from the two missions on 10 September reveal shallow lifting up to about 600 hPa. Presuming that such lifting was also occurring before the first mission, it is consistent with the observation of a shallow cyclonic circulation on 10 September. On 11 September, the large MCS that

<sup>9</sup> DCAPE can be defined as a negative quantity since the buoyancy is negative, but we define it as positive here.

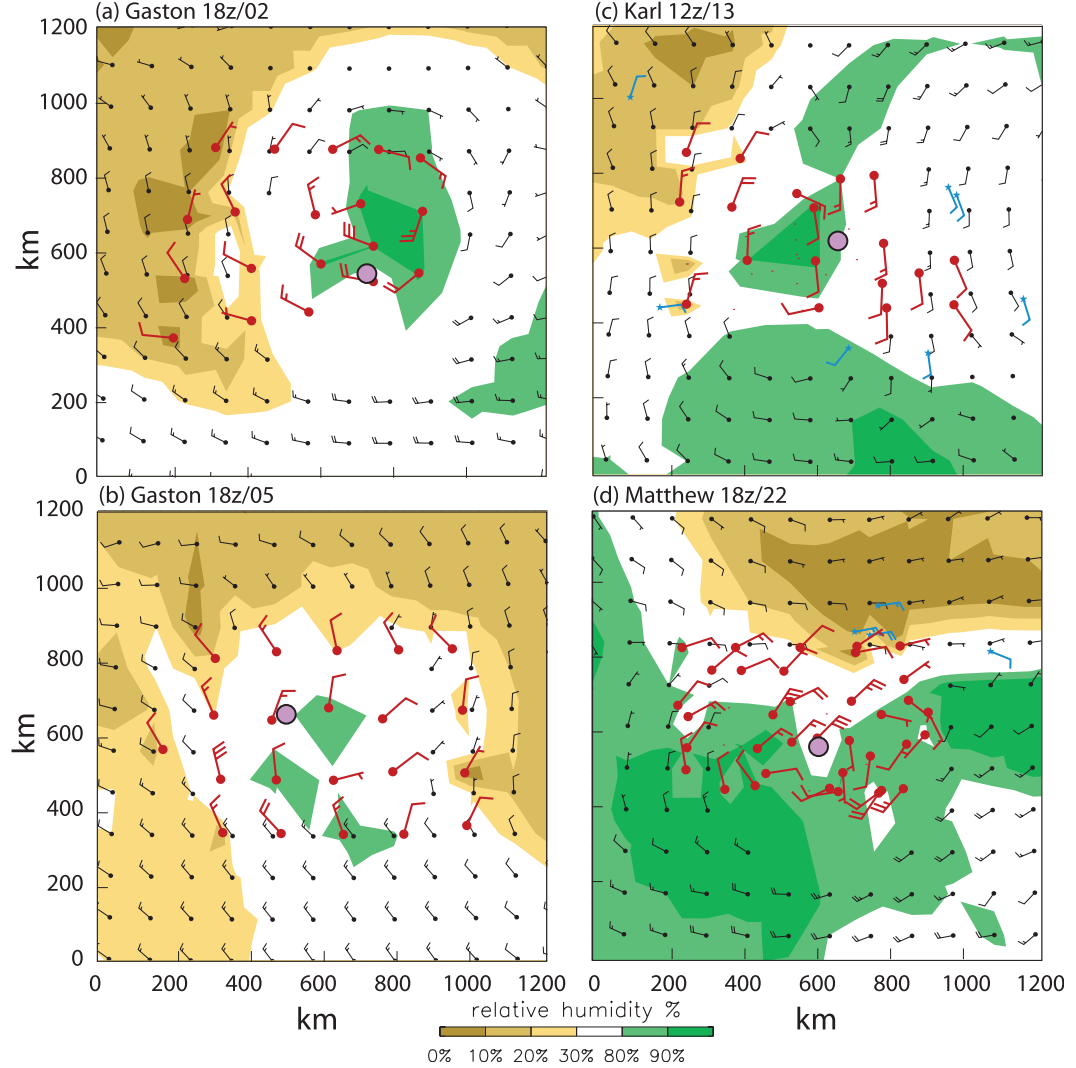


FIG. 15. Analyzed relative humidity at 500 hPa along with winds from GFS analysis (black) and dropsonde winds (red) and cloud drift winds (blue) for (a) Gaston at 1800 UTC 2 Sep, (b) Gaston at 1800 UTC 5 Sep, (c) Karl at 1200 UTC 13 Sep, and (d) Matthew at 1800 UTC 22 Sep. Violet circle indicates location of circulation center at 900 hPa. GFS humidity data within 300 km of the model-based consensus center location were not used in the relative humidity analysis, nor were GFS winds plotted within this radius.

develops to the west of the circulation at 900 hPa projects onto ascent above 600 hPa, consistent with a mature or decaying convective system, which was the case (Fig. 4e). On 12 September, there is strong ascent, consistent with the vigorous convection on this day (Fig. 6c). Deep ascent is again apparent at 1200 UTC 13 September when convection activity is increasing, but 0000 and 2100 UTC profiles from the same day reveal essentially no ascent between 850 and 600 hPa. At these times there was minimal convection activity (Fig. 4e). Finally, deep lifting occurs at 1800 UTC 14 September, near the time of genesis, when convection is again increasing in coverage and intensity.

Vertical motion profiles for Matthew indicate subsidence at 1500 UTC on 20 and 21 September; however, the profiles on these two days are relatively uncertain, due mainly to suboptimal sampling by the GV and DC-8 that resulted from air space restrictions. Much better spatial sampling occurred on 22 September, one day prior to genesis, and the profile is characterized by deep ascent. The dropsonde pattern on 23 September did not allow the computation of a vertical motion profile. On 24 September, little ascending motion is apparent over the center. This could be due to the sampling, and also to the displacement of the strongest convection from the center in vertical shear (Fig. 7e).

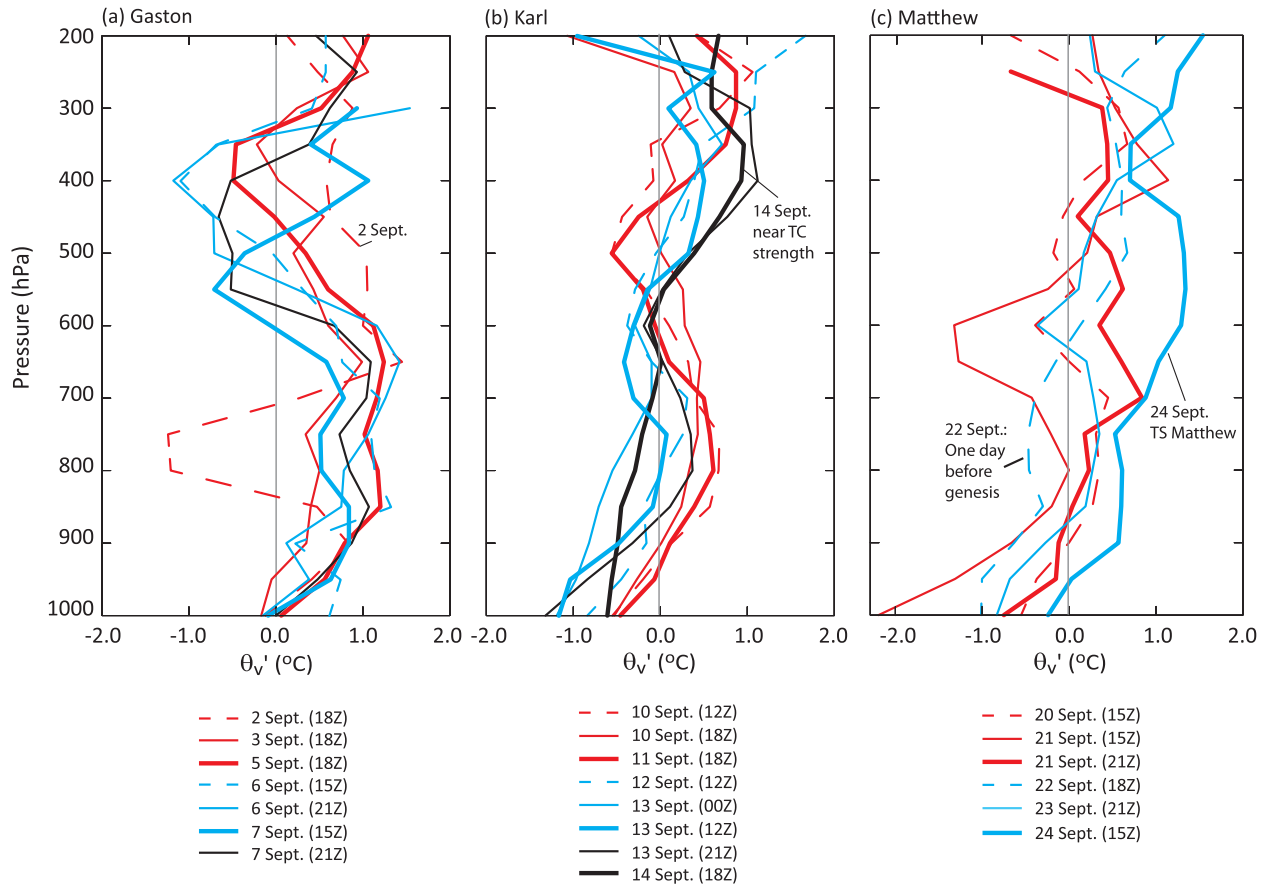


FIG. 16. Profiles of virtual potential temperature anomalies at different times, where the reference profile is the average of dropsondes from  $3^{\circ}$  to  $6^{\circ}$  radius from the 900-hPa circulation center.

## 5. Conclusions

We have presented an analysis of satellite and dropsonde data for three Atlantic tropical weather systems observed during 2010: Gaston, after it had weakened from tropical storm strength, Karl for five days leading

to TC formation, and Matthew before, during, and after TC formation. The objective of the analysis was to explain why Gaston failed to redevelop and why Karl and Matthew developed when and where they did. While complete answers to these questions, and more general questions about genesis, are difficult to unambiguously

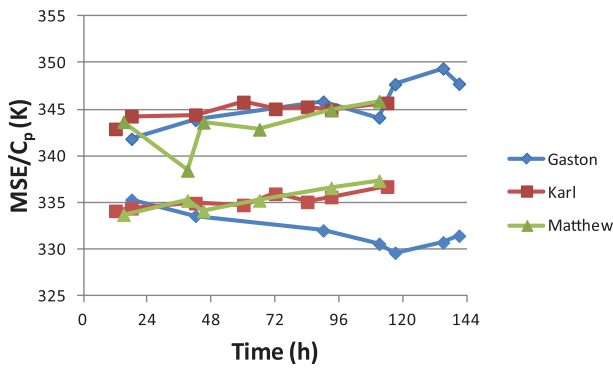


FIG. 17. Moist static energy (normalized by  $C_p$ ; K) vs time (h) at 950 hPa (upper set of three curves) and 500 hPa (lower set of three curves), computed from dropsondes within  $3^{\circ}$  from the 900-hPa circulation center.

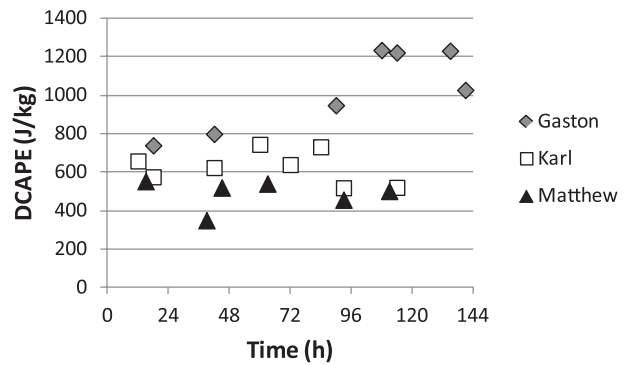


FIG. 18. Downdraft CAPE ( $\text{J kg}^{-1}$ ) vs time (h). Values are averaged within  $3^{\circ}$  from the center of circulation at 900 hPa.

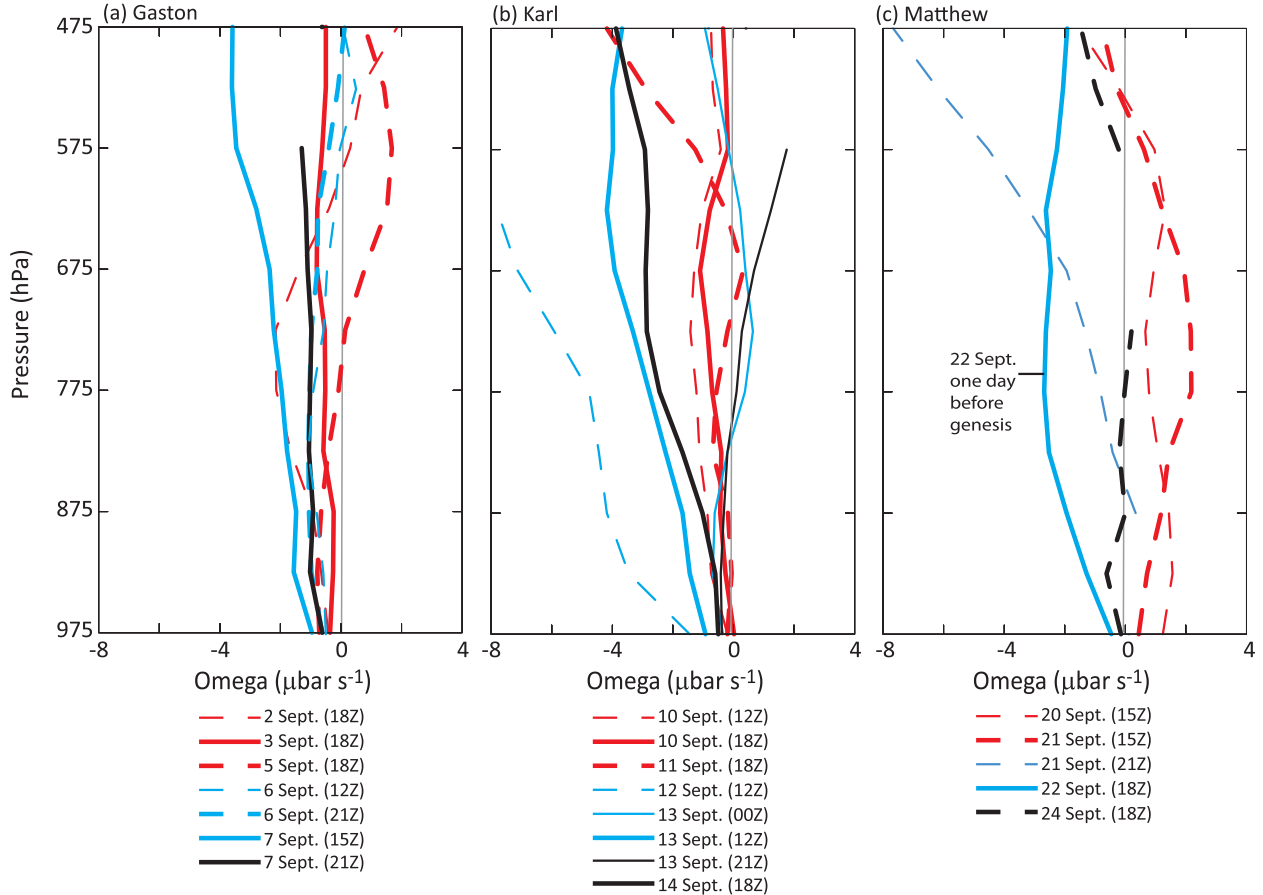


FIG. 19. Omega (“pressure vertical velocity”;  $\mu\text{bar s}^{-1}$ ) computed from vertically integrating the divergence obtained from radial wind component (relative to 900-hPa center) averaged within  $3^\circ$  radius from the 900-hPa center. Dashed contours are used for the more uncertain half of the profiles (this figure only).

state based solely on the preceding analysis, there are nonetheless several indicative findings.

The vertical alignment of mesoscale cyclonic circulations, coupled with quasi-persistent deep moist convection, appears essential for the formation of Karl and Matthew, but these two factors did not exist simultaneously in Gaston (after it weakened from tropical storm strength). The importance of vertical alignment is noted by D09, Raymond and López Carrillo (2011), and Rappin et al. (2010). Misalignment leads to strong relative flow in addition to what might be imposed through environmental vertical wind shear. Strong relative flow makes the overall system extremely vulnerable to any dry air that exists nearby (as in Gaston).

Deep moist convection, together with vertical shear, influences vertical alignment in important ways. The misalignment that occurred in Karl on 11 September arose from convection on the downshear side of the lower-tropospheric circulation, which spun up a midtropospheric vortex displaced from the low-level center. A process not completely understood is how deep convection

managed to align the circulations in Karl against the shear. Some clues may be provided by Molinari and Vollaro (2010) in their study of Hurricane Gabrielle (2001), in which convection is vigorous enough (possibly because of the shear itself) that an entirely new circulation center forms beneath the midtropospheric vortex. Rappin et al. (2010) and Rappin and Nolan (2012) show a similar downshear alignment process in idealized simulations. They also stress that this process depends strongly on environmental conditions.

Vertical shear in Gaston briefly aligned the vortex on 3 September, but it appears that convection was too weak to intensify the vortex (SM). Based on mass flux profiles that indicated weak, shallow ascent rather than the characteristic “top-heavy” profiles of mature organized convective systems (Houze 1989), it is probable that the extent and depth of convection were limited directly by dry air entrainment, as emphasized in Braun et al. (2012). The misalignment of the vortex in Gaston due to shear, coupled with a lack of convection sufficient to rebuild the vortex, resulted in a systematic decay of the vortex from

the middle troposphere downward. However, dry air in the middle troposphere also created a greater potential for downdrafts in Gaston compared to other cases, assuming convection could tap this potential. Downdrafts may have become more important by 7 September when the convective activity began increasing, although there is relatively scant evidence for this in the thermodynamic data (Fig. 16a).

The two developing cases featured relatively faster growth of the midtropospheric circulation prior to genesis compared to the lower-tropospheric circulation, consistent with the findings of Raymond et al. (2011) for developing disturbances over the western Pacific Ocean. The lower tropospheric circulation subsequently increased rapidly as the system transitioned into a tropical cyclone. We also observed moistening of the middle troposphere (600–400 hPa) prior to genesis. While moistening of the lower troposphere was not obvious, there was evidence of cooler air in lowest kilometer in these cases, which may have arisen from mesoscale downdrafts. In addition, there was preferential warming in the middle and upper troposphere prior to genesis and thus a stabilization of the profile, contrasting with the destabilization in Gaston. This overall behavior resembles that discussed in Raymond and Sessions (2007), in which the “efficiency” with which lower tropospheric convergence could be induced (and hence vortex spinup) increased with increasing stabilization in the middle troposphere. This thermodynamic state encourages maximum upward motion at a relatively low altitude, as seen in the more reliable profiles of vertical motion. This low-level ascent enhances vortex stretching in the lower troposphere and spinup of a near-surface cyclonic circulation. A strong midtropospheric vortex and deep saturation were emphasized by Nolan (2007) as conditions favoring genesis (and rapid intensification). Pronounced moistening and slight warming in the middle troposphere were noted by Montgomery and Smith (2011) and Raymond et al. (2011) in the genesis of Typhoon Nuri (2008). Generally consistent with these previous results, the clearest signals prior to genesis are vortex alignment, middle-tropospheric moistening, greater increase of the midtropospheric cyclonic circulation, and warming in the middle and upper troposphere.

The relatively cool air that we find in the lower troposphere for Karl and Matthew is similar to but not as deep as that found by Bister and Emanuel (1997), but more extensive than found by Montgomery and Smith (2011). Further, SM reported no cool anomaly in the lower troposphere in the same three cases analyzed herein. Much of the difference in the present cases results from how anomalies are defined. SM considered all dropsondes, rather than dropsondes only within  $3^{\circ}$  of the

circulation center, and used a time-averaged reference profile rather than the average of contemporaneous data in a ring surrounding the  $3^{\circ}$  inner region as we have done. Because convection is more often found near the comoving circulation center than elsewhere, it is not surprising that we find relatively cool air in this inner region. Bister and Emanuel focused even more locally on a mesoscale convective system, and this may explain the greater temperature perturbation they reported (a point made by SM). Negative virtual temperature perturbations are not seen near the surface in Gaston presumably because convection was much less widespread than in Karl and Matthew. Furthermore, because of the time-varying reference profile used herein, the near-surface virtual temperature perturbations in Gaston are nearly zero, despite the fact that Gaston traversed increasing sea surface temperature with time.

Regarding the marsupial paradigm, we note recurring mesoscale structure in the convection that is focused near the center of the circulation in the comoving frame (Figs. 5–7). The repeatable mesoscale organization of convection that is observed in each of the three cases studied herein suggests a strong constraint perhaps from both rotation (the pouch) and vertical shear. This contrasts with the notion of convection distributed in a quasi-random manner, and it further implies a certain degree of predictability of genesis as was already alluded to in D09.

Deep, moist convection pulsates with a quasi-diurnal period in the cases observed. While the mechanism(s) governing the convection cycle are left for future investigation, it is clear from our analysis that a favorable mass flux profile for the intensification of circulation in the lower troposphere exists for only a portion of the diurnal cycle and that relatively long periods exist with minimal convection and weak mass flux. To achieve genesis, each successive burst of convection must overcompensate for the probable weakening during convection lulls due to effects such as vertical shear and friction. A spatial structure of convection that is relatively consistent, in the comoving frame, from one cycle to the next could be an important factor that allows genesis to occur after a small number of convective cycles.

Further analysis of these and other cases observed during PREDICT, combined with modeling studies in which various factors distinguishing these cases can be targeted, are needed to extend the present analysis. In particular, the details at the convective scale have not been addressed in the present study. A variety of in situ and remote sensing data collected on the GV, NASA aircraft, and the NOAA P-3 will be indispensable for investigating finer scales of motion, while the present study offers a mesoscale context for those observations.

**Acknowledgments.** The authors wish to acknowledge the staff of the Earth Observing Laboratory of NCAR for their support of PREDICT, plus helpful discussions with Drs. Michael Montgomery and Michael Bell of Naval Postgraduate School in Monterey, Lance Bosart from the University at Albany SUNY, and Clark Evans and Brian Tang from NCAR during the course of this work. The manuscript also benefitted from comments by Dave Raymond from New Mexico Tech., Scott Braun from NASA GFSC, David Nolan from the University of Miami, and an anonymous reviewer.

## REFERENCES

- Bister, M., and K. A. Emanuel, 1997: The genesis of Hurricane Guillermo: TEXMEX analyses and a modeling study. *Mon. Wea. Rev.*, **125**, 2662–2682.
- Braun, S. B., J. A. Sippel, and D. S. Nolan, 2012: The impact of dry midlevel air on hurricane intensity in idealized simulations with no mean flow. *J. Atmos. Sci.*, **69**, 236–257.
- Davis, C. A., and S. B. Trier, 2007: Mesoscale convective vortices observed during BAMEX. Part I: Kinematic and thermodynamic structure. *Mon. Wea. Rev.*, **135**, 2029–2049.
- , C. S. Snyder, and A. C. Didlake Jr., 2008: A vortex-based perspective of eastern Pacific tropical cyclone formation. *Mon. Wea. Rev.*, **136**, 2461–2477.
- Dunkerton, T. J., M. T. Montgomery, and Z. Wang, 2009: Tropical cyclogenesis in a tropical wave critical layer: Easterly waves. *Atmos. Chem. Phys.*, **9**, 5587–5646.
- Emanuel, K. A., 1994: *Atmospheric Convection*. Oxford University Press, 580 pp.
- Gilmore, M. S., and L. J. Wicker, 1998: The influence of mid-tropospheric dryness on supercell morphology and evolution. *Mon. Wea. Rev.*, **126**, 943–958.
- Gray, W. M., 1998: The formation of tropical cyclones. *Meteor. Atmos. Phys.*, **67**, 37–69.
- Halverson, J., and Coauthors, 2007: NASA's Tropical Cloud Systems and Processes Experiment. *Bull. Amer. Meteor. Soc.*, **88**, 867–882.
- Hendricks, E. A., M. T. Montgomery, and C. A. Davis, 2004: The role of “vortical” hot towers in the formation of Tropical Cyclone Diana (1984). *J. Atmos. Sci.*, **61**, 1209–1232.
- Hirose, M., R. Oki, S. Shimizu, M. Kachi, and T. Higashiuwatoko, 2008: Finescale diurnal rainfall statistics refined from eight years of TRMM PR data. *J. Appl. Meteor. Climatol.*, **47**, 544–561.
- Houze, R. A., 1989: Observed structure of mesoscale convective systems and implications for large-scale heating. *Quart. J. Roy. Meteor. Soc.*, **115**, 425–461.
- Joyce, R. J., J. E. Janowiak, P. A. Arkin, and P. Xie, 2004: CMORPH: A method that produces global precipitation estimates from passive microwave and infrared data at high spatial and temporal resolution. *J. Hydrometeor.*, **5**, 487–503.
- Molinari, J., and D. Vollaro, 2010: Rapid intensification of a sheared tropical storm. *Mon. Wea. Rev.*, **138**, 3869–3885.
- Montgomery, M. T., and R. K. Smith, 2011: The genesis of Typhoon Nuri as observed during the Tropical Cyclone Structure (2008) (TCS08) field experiment. Part 2: Observations of the convective environment. *Atmos. Chem. Phys. Discuss.*, **11**, 31 115–31 136.
- , M. E. Nicholls, T. A. Cram, and M. E. Saunders, 2006: A vortical hot tower route to tropical cyclogenesis. *J. Atmos. Sci.*, **63**, 355–386.
- , and Coauthors, 2012: The Pre-Depression Investigation of Cloud Systems in the Tropics (PREDICT) Experiment: Scientific basis, new analysis tools and some first results. *Bull. Amer. Meteor. Soc.*, **93**, 153–172.
- Nolan, D., 2007: What is the trigger for tropical cyclogenesis? *Aust. Meteor. Mag.*, **56**, 241–266.
- Ooyama, V., 1982: Conceptual modeling of the theory and evolution of the tropical cyclone. *J. Meteor. Soc. Japan*, **60**, 369–380.
- Rappin, E. D., and D. S. Nolan, 2012: The effect of vertical shear orientation on tropical cyclogenesis. *Quart. J. Roy. Meteor. Soc.*, doi:10.1002/qj.977, in press.
- , —, and K. A. Emanuel, 2010: Thermodynamic control of tropical cyclogenesis in environments of radiative-convective equilibrium with shear. *Quart. J. Roy. Meteor. Soc.*, **136**, 1954–1971.
- Raymond, D. J., and H. Jiang, 1990: A theory for long-lived mesoscale convective systems. *J. Atmos. Sci.*, **47**, 3067–3077.
- , and S. Sessions, 2007: Evolution of convection during tropical cyclogenesis. *Geophys. Res. Lett.*, **34**, L06811, doi:10.1029/2006GL028607.
- , and C. López Carrillo, 2011: The vorticity budget of developing Typhoon Nuri (2008). *Atmos. Chem. Phys.*, **11**, 147–163.
- , —, and L. L. Cavazos, 1998: Case-studies of developing east Pacific easterly waves. *Quart. J. Roy. Meteor. Soc.*, **124**, 2005–2034.
- , S. L. Sessions, and C. López Carrillo, 2011: Thermodynamics of tropical cyclogenesis in the northwest Pacific. *J. Geophys. Res.*, **116**, D18101, doi:10.1029/2011JD015624.
- Reasor, P. D., M. T. Montgomery, and L. D. Grasso, 2004: A new look at the problem of tropical cyclones in vertical shear flow: Vortex resiliency. *J. Atmos. Sci.*, **61**, 3–22.
- Riemer, M., and M. T. Montgomery, 2010: Simple kinematic models for the environmental interaction of tropical cyclones in vertical wind shear. *Atmos. Chem. Phys. Discuss.*, **10**, 28 057–28 107.
- Ritchie, E. A., and G. J. Holland, 1997: Scale interactions during the formation of Typhoon Irving. *Mon. Wea. Rev.*, **125**, 1377–1396.
- Simpson, J., E. A. Ritchie, G. J. Holland, J. Halverson, and S. Stewart, 1997: Mesoscale interactions in tropical cyclone genesis. *Mon. Wea. Rev.*, **125**, 2643–2661.
- Sippel, J. A., and F. Zhang, 2008: A probabilistic analysis of the dynamics and predictability of tropical cyclogenesis. *J. Atmos. Sci.*, **65**, 3440–3459.
- Sorooshian, S., X. Gao, K. Hsu, R. A. Maddox, Y. Hong, H. V. Gupta, and B. Imam, 2002: Diurnal variability of tropical rainfall retrieved from combined GOES and TRMM satellite information. *J. Climate*, **15**, 983–1001.
- Tory, K. J., and W. M. Frank, 2010: Tropical cyclone formation. *Global Perspectives on Tropical Cyclones: From Science to Mitigation*, J. C. L. Chan and J. D. Kepert, Eds., World Scientific, 55–91.
- Yang, G.-Y., and J. Slingo, 2001: The diurnal cycle in the tropics. *Mon. Wea. Rev.*, **129**, 784–801.